Alzheimer disease: The proposed role of tanycytes in the formation of tau tangles and amyloid beta plaques in human brain

Short title: Tanycyte-mediated waste removal from the brain

Ruth Fabian-Fine[1*], Abigail G. Roman[1] and Adam L. Weaver[1]

[1] Department of Biology, Saint Michael's College, Colchester, VT 05439, USA

* Corresponding author

E-mail: rfabianfine@smcvt.edu (RF)

Abbreviations

Aquaporin-4 aqua channel (AQP4)

Alzheimer Disease (AD)

Amyloid beta (Aß)

Amyloid Precursor Protein (APP)

Glial Fibrillary Acid Protein (GFAP)

Immunoreactive (IR)

Presenilin-1 (Pres1)

Abstract

Currently, the causes for Alzheimer Disease (AD) are thought to lie in the formation of abnormal protein deposits including tau tangles and Amyloid ß (Aβ) plaques in the human cortex. These proteins are believed to accumulate in the brain due to impaired waste removal resulting in neurodegeneration. In an alternative hypothesis we have recently proposed the existence of an aquaporin4 aqua channel (AQP4)-expressing tanycyte-derived canal network that likely internalizes waste for removal from the brain. We propose that both Aβ and tau protein may play important structural roles in this canal system. In support of this hypothesis, we demonstrate the formation of waste-internalizing receptacles by AQP4-expressing myelinated tanycytes. Using RNA-scope *in situ* hybridization, immunohistochemistry, ultrastructural, and histological approaches, we demonstrate receptacle differentiation in tanycyte-derived 'swell-bodies.' We show that these receptacles are AQP4- and Aβ-immunoreactive and that related gene expression is observed in 'swell-bodies' where receptacle differentiation is observed. Through correlative light- and electron-microscopy in human and mouse brain, we demonstrate that both Aß and tau protein are associated with these waste-internalizing structures [1] and likely play important roles in the waste internalization process. Based on our findings, we postulate that the functional significance of Aß may be structural stabilization of waste-internalizing structures and canals to prevent their collapse during the uptake process. We propose that tau protein may govern the quantitatively appropriate release of waste-internalizing structures. We postulate that AD-related Aβ-plaques and tau tangles likely show hypertrophic pathologies of this glial-canal-system and associated waste-internalizing receptacles.

Introduction

Currently, the underlying causes for Alzheimer Disease (AD) are elusive and are thought to lie in the formation of abnormal intracellular deposits of hyperphosphorylated tau tangles and extracellular Amyloid ß (Aß) plaques throughout the human cortex. Due to this abnormal protein accumulation in AD-affected brain tissue, a prevalent causative hypothesis is failed waste removal from the nervous system [2-5]. Currently, the way by which waste is cleared from the brain is poorly understood. Illiff et al. (2012) have

48 proposed the existence of an aquaporin-4 aqua channel (AQP4)-mediated 'Glymphatic System.' Based on
49 this postulation AQP4-expressing astrocytes are thought to flush cellular debris from the brain by means of
50 a cytoplasmic convective flow of cerebrospinal fluid. Using two-photon microscopy and fluorescent tracers
51 in mouse brain, the authors demonstrated the formation of a convective flow through the neuropil believed
52 to flush cellular waste into peri-venous spaces for clearance from the brain [2, 6-8]. Interestingly, a
53 significantly reduced flow of cerebrospinal fluid was observed in AQP4-null mice compared to wild-type
54 mice [9]. However, this hypothesis has been put into question predominantly regarding the proposed
55 astrocyte-induced AQP4-mediated flow of brain fluids [4, 10]. In an alternative model for waste removal
56 from the brain, we have proposed that debris uptake may be mediated by a 'glial-canal system.' We
57 postulate that this tanycyte-derived canal system is highly conserved between spider, rodent, and human
58 brain and internalizes waste for removal from the brain parenchyma [11]. We propose that myelinated
59 AQP4-expressing ependymal tanycytes form a syncytial network and contact neurons and glial cells for
60 proposed waste removal via differentiating waste-internalizing receptacles. We have provided evidence
61 that this canal system is structurally impaired in degenerating brain tissue. This structural impairment is
62 manifested in the form of hypertrophic tanycyte swelling that leads to catastrophic obstruction, cytoplasmic
63 depletion, and death of neurons. We have termed this macroglia-induced cell death 'gliaptosis' [11].

64 To test our postulation that ependymal tanycytes internalize cellular matter, here we have conducted
65 RNAscope gene expression together with immunohistochemical, histological, and ultrastructural studies.
66 To support our postulations, we have furthermore conducted functional studies on living mouse brain to
67 assess whether structures we have identified as waste-receptacles internalize fluorochromes as predicted.
68 We provide evidence that these receptacles express the Aß-related genes for presenilin-1 (Pres1) and
69 amyloid precursor protein (APP) and appear immunolabeled for Aß. We furthermore demonstrate that these
70 receptacles swell in AD-affected brain tissue and resemble Aß-plaques [12] in immunolabeled sections.
71 Offering an alternative hypothesis we postulate that lining of waste-internalizing receptacles and canals by
72 structurally stable Aß aggregates [13] may provide structural stabilization of these waste-internalizing
73 structures to prevent their collapse during AQP4-mediated waste intake.

74 # Materials & methods

Experimental models and study participant details

Mouse brain tissue

The mouse brain originated from adult (6- to 15-month-old) female wildtype strain is Cdh5-GCaMP8 mice. For ethical reasons and to avoid unnecessary animal sacrifices, the brains used in this study were obtained from surplus tissue. The tissue was obtained freshly upon dissection of the animals and processed as described below. IACUC approval was granted under PROTO202200018 (University of Vermont) and IACUC-2024-001 Fabian-Fine (Saint Michael's College).

Human brain tissue

The human brain tissue used for our investigations originated from tissue used in a previous study [11]. As stated in this publication, the tissue was fully written consented, including 'consent for research,' from next of kin in compliance with Vermont State law, the Health and Human services regulation 45 CFR 46.102(e), and the University of Vermont regulations regarding human subjects research. In brief: The tissue originated from four Caucasian decedents. The autopsy examination was carried out by Dr. John DeWitt at the University of Vermont Medical Center in the context of a previously published study [11]. The tissue samples of AD-decedents were consistent with high (86-year-old female) and intermediate (86-year-old male) burdens of ADNC (for more detail, see [11]).

Experimental design and statistical analysis

Uptake experiments on living mouse brain

Three mice from which the surplus brain tissue was obtained were euthanized with Euthasol (Virbac) by a licensed technician. The brains were immediately removed from the cranium and transferred into mouse culture medium DMEM (VWR Cat #45000-312) containing 4.5 g/L glucose, L-glutamine, 10% Fetal Bovine Serum and 1% Penicillin/Streptomycin at 37 °C to maintain temperature appropriate enzymatic activity. The two brain hemispheres were separated, and each hemisphere was sliced into three equal coronal sections along the anterior-posterior axis. The sections from the right hemisphere (controls) were kept in culture

99 medium, whereas the left hemisphere sections (experimental) were kept in culture medium to which we
100 added Cy3-coupled goat-anti rabbit secondary antibody (Jackson ImmunoResearch # 111 -165-003). After
101 30 min, both control and experimental brain sections were fixed with freshly made 4% paraformaldehyde
102 (4% PFA) overnight at 6 °C. The preparations were embedded in 4% agarose (Sigma 9539) and sectioned
103 into 70-µm vibratome sections using a Leica Vibratome 1000S. The sections were washed in PBS and
104 mounted on glass slides using Mowiol (Sigma 81381). The sections of both control and experimental
105 preparations were imaged with identical settings using a Zeiss Axio-Imager confocal microscope with ZEN-
106 Blue software. To test that the internalized fluorochrome detected in ependymal cells of the experimental
107 preparations indeed originate from the Cy3-coupled goat antibody, we utilized a secondary Alexa 488-
108 coupled donkey anti-goat antibody (Jackson ImmunoResearch # 705-545-003). For this purpose, additional
109 sections were cut and washed in 0.1 M phosphate-buffered saline pH 7.4 (PBS). Unspecific binding sites
110 were blocked with blocking medium containing 0.25% Bovine Serum Albumin (Sigma A4503) and 5%
111 Normal goat serum (Sigma G9023) in 1% Triton-X/PBS for 20 min prior to incubation with the donkey anti-
112 goat antibody (1:600 overnight at 6 °C). Subsequently, the preparations were washed in PBS (2x5 min),
113 stained with Hoechst Blue nuclear stain (1:3000; 15 min), washed in PBS 5x10 min, and mounted on glass
114 slides using Mowiol prior to examination with the Zeiss confocal microscope.

115 Image and statistical analysis

116 Confocal images were exported from the Zeiss ZEN-Blue program using the “Original Data” setting and
117 analyzed in CellProfiler 4.2.8 for all measurements [14]. Briefly, Cy3 stained objects were identified [Three-
118 class Otsu thresholding; middle class: background] that were brighter than the background and had a
119 diameter between 5 and 60 µm. Object size/shape and intensity were measured. In some cases, full
120 captured images had their exposure minimally modified to enhance contrast or brightness identically for
121 figures, but not for the analysis.

122 An unpaired, two-tailed Student’s t-test with Welch’s correction was used to perform comparisons of the
123 Log_{10} mean object intensities across control (0 µM) and TGN-020 AQP4-blocked (60 µM; Sigma SML0136)
124 conditions. All statistical parameters and results are reported in the relevant figure legend. To the best of

125 our knowledge, all assumptions of this test were met. Statistics were calculated and graphs were created
126 using Prism 10.4.1 (GraphPad Software).

127 Tissue processing for semi- and ultrathin sectioning

128 Hippocampal tissue samples (~50 mm thick) were immersed in freshly prepared ice cold 4%
129 paraformaldehyde (EMS 15710) and 2.5% glutaraldehyde (EMS 16019) in phosphate buffered saline (pH
130 7.4, 0.1 M; PBS) and fixed for at least 48 hours in the refrigerator. The preparations were embedded in 4%
131 agarose and sectioned, postfixed in 1% osmium tetroxide, dehydrated in a graded series of ethanol, and
132 embedded into Araldite as described previously [11]. Using a Diatome Histo-knife with 8 mm blade ultrathin
133 sections (50-60 nm) were cut with a Leica Ultracut E.

134 The sections were stretched with chloroform (Electron Microscopic Sciences 12540) by gently waving a
135 chloroform-soaked wooden toothpick over the sections without touching them until they were sufficiently
136 stretched. The sections were collected on pioloform-coated single-slot copper grids (EMS G2010CU) using
137 #5 Dumont forceps and an eyelash that was mounted to a wooden toothpick using hot bee's wax. Grids
138 were contrasted with aqueous 1.5% uranyl acetate (6 min) and Reynold's lead citrate (6 min) according to
139 standard electron microscopic methods. The examination was conducted using a JOEL 1400 electron
140 microscope with digital image acquisition operated at 80 kV.

141 Light microscopic immunohistochemistry

142 Human hippocampal tissue utilized for light-microscopic immunolabeling was fixed in freshly prepared, ice-
143 cold 4% paraformaldehyde for a minimum of 48 h at 6 °C. The tissue was embedded in 4% Agarose,
144 sectioned into 70-µm vibratome sections using a Leica Vibratome 1000S. The sections were washed in
145 PBS 4x5 min and unspecific binding sites were blocked with blocking medium containing 0.25% Bovine
146 Serum Albumin (Sigma A4503) and 5% Normal goat serum (Sigma G9023) in 1% Triton-X/PBS for 20 min.
147 The sections were incubated overnight at 6 °C within the respective primary antibody solutions (rabbit anti-
148 aquaporin-4 antiserum BiCell 20104, rat anti-Caspase2 BiCell 10302, Anti-Pres1; Sigma Aldrich ZRB1614,
149 Anti-APP-C99; Sigma Aldrich MABN380, mouse anti-α-tubulin 12G10, DSHB, IOWA, and anti-Myelin 6-
150 4H2 DSHB, IOWA) at dilutions of 1:100. Prior to incubation with the secondary antibodies, preparations

151 were washed thoroughly in PBS (5x10 min), incubated in blocking medium as described above, and
152 incubated with either secondary Cy3 goat anti-rabbit (Jackson ImmunoResearch Laboratories 111-165-
153 003), Cy3 goat anti-mouse (Jackson ImmunoResearch # 115-165-148), and Cy3 goat-anti rat (Jackson
154 ImmunoResearch # 112-165-003) at dilutions of 1:600 in PBS containing 10% blocking medium overnight
155 at 6 °C. Subsequently, the sections were rinsed in PBS (3x2 min). For the nuclear stain, we utilized Hoechst
156 Blue (Sigma Aldrich 94403-1ML) at a dilution of 1:3000 in PBS for 20 min. After washing in PBS (5x10 min),
157 the sections were mounted on glass slides using Mowiol (Sigma 81381). To avoid bleaching of the
158 fluorochromes, the mounting was conducted with minimum illumination.

159 Immunoperoxidase stain for Aβ and Tau protein

160 Immunolabeling for both A*β* and Tau 8 were conducted on paraffin embedded 8-µm sections as previously
161 described [11].

162 Luxol H&E staining of Autopsy Tissue

163 The histological staining methods were carried out as previously described [11].

164 RNA-scope in situ RNA hybridization

165 The RNA-scope methods to detect APP, AQP4 and Pres1-RNA expression were carried out as described
166 previously [11].

167 Light microscopic image acquisition

168 Histological brain sections were examined and captured using an Olympus light microscope with digital
169 image acquisition. Figures were created using Adobe Photoshop and Illustrator.

170 RNAscope control experiments

171 The RNA integrity in the human brain tissue was tested in all samples. We used in situ hybridization for the
172 human 'housekeeping' gene peptidylpropyl isomerase B, which is expressed at low levels. The observed
173 expression of this gene thus demonstrated sufficient preservation of RNA in our tested brain samples. For

174 negative controls, the bacterial gene dapB was utilized. The absence of fluorescent signals in the negative
175 control supports the specificity of our detected AQP4, Pres1, GFAP and APP-RNA expression signals.

176 ## Immunohistochemistry negative controls

177 The antibodies utilized here have been well-established in the human brain. We have routinely carried out
178 negative controls in which the primary antibodies were omitted to exclude that the observed strong
179 fluorescence may be attributed to autofluorescence in the tissue.

180 # Results

181 ## Aquaporin-4 and myelin double-labeled ependymal tanycytes
182 ## form 'swell-bodies'

183 In both mouse and human hippocampus ependymal tanycytes whose somata reside in the
184 temporal horn of the lateral ventricles form an extensive network of long, myelinated, slender processes
185 (indicated by Luxol-blue stain in Fig 1A, B) that emanate from the alveus and project into the hippocampal
186 stratum pyramidale (Fig 1E). In both human and mouse hippocampus, the AQP4-immunolabeled nature of
187 these myelinated, slender processes is apparent (Fig 1C, D, J-K). It is likely this AQP4-expressing nature
188 of tanycytes that leads to water influx into these glial cells that explains different swelling patterns in
189 individual tanycyte processes (Fig 1H, see discussion). Both Luxol-blue stain in human hippocampus (Fig
190 1H) and double immunolabeling for AQP4 and myelin in mouse hippocampus (Fig 1I-K) show myelin-
191 labeled circular structures that line the inside of these glial processes reminiscent of stabilizing cartilaginous
192 rings in trachea (Fig 1 H-K; see discussion).

193 Another organelle type that is formed along AQP4-expressing myelinated tanycyte processes are
194 circular electron lucent 'swell-bodies.' These organelles are clearly visible in Luxol H&E-stained human
195 hippocampus and AQP4/myelin immunolabeled mouse hippocampus (Figs 1; 2A-D). Each swell body
196 contains between one and six circular organelles that stain for nuclear stain and appear physically
197 associated with myelinated tanycyte processes (Fig 1O-T). Unlike typical cell nuclei, these organelles give

198 rise to receptacles that internalize electron-dense waste (Figs 1Q, S, T; 2A-D; see also below). Due to three
199 distinct characteristics that distinguish these nucleus-like structures from conventional cell nuclei, we will
200 refer to these nucleus-like structures as 'tanysomes.'

201 Tanysome versus conventional cell nucleus

202 Despite the positive nuclear stain, three main features distinguish tanysomes from conventional nuclei
203 found in cell bodies. These features can be observed in both non-AD affected and AD-affected tissue and
204 include: *(i)* the emergence of the aforementioned varicose waste-receptacles from these organelles (Fig 1
205 S, T; see more detail below), *(ii)* our observation that these nucleus-like organelles are physically connected
206 with myelinated tanycyte processes (Figs 1, 2), and *(iii)* the emergence of swelling toroid-shaped structures
207 from tanysomes (Figs 1R; 2). These membranous ring structures swell to widely varying diameters of >20
208 µm. Interestingly, they stain for anti-phosphorylated tau protein, anti-α-tubulin, anti-Aβ, anti-AQP4, anti-
209 myelin and Luxol-blue H&E stain (Fig 2). Like tanysomes from which toroids emerge, the latter often stain
210 for nuclear stain and give rise to varicose receptacles (Fig 2M).

211 Tanysomes and tanycyte processes give rise to waste-
212 internalizing myelin-derived waste receptacles

213 The lumina of swell-bodies that are void of receptacles appear clear at the light microscopic level in Luxol
214 H&E-stained preparations and electron lucent at the electron microscopic level (Fig 1O) unlike the
215 structured cytoplasmic appearance in neuronal and glial cell somata (Fig 1O). In other swell-bodies
216 tanysome derived membranous structures give rise to interconnected membrane networks that
217 predominantly originate from tanysomes and form swelling donut-shaped structures (Fig 2 H, I; in the
218 following referred to as 'toroids') and circular receptacles (Fig 2D; for more detail see below). Electron-
219 microscopic examination reveals the formation of receptacles that emanate from tanysomes (Fig 1Q, R).
220 The appearance and diameters of these receptacles vary widely from electron-lucent with diameters of ~20
221 nm to electron-dense with diameters of up to 1 µm (Fig 1Q, T, for more detail see below). The blue coloration

222 of larger receptacles in Luxol H&E-stained human brain preparations is suggestive of their myelinated
223 nature (Fig 2C, D; more detail is provided in Fig 6).

224 Tanycyte-derived receptacles project into neuronal somata

225 Immunolabeling demonstrates the AQP4-IR nature of waste receptacles that emanate from tanysomes (Fig
226 3A). Investigation of Luxol H&E-stained brain sections show strands of Luxol-blue stained waste
227 receptacles that emanate from tanysomes project into neuronal somata in both AD-affected and AD-
228 unaffected human hippocampus (Fig 3C-G). Please note the close association of the swell body with the
229 neuronal somata in non-AD affected tissue, which leads to a convex indentation consistent with hydrostatic
230 pressure exerted on the soma (Fig 3G). In AD-affected brain tissue, the receptacles appear hypertrophic
231 compared to non-AD-affected tissue (Fig 3). These findings are consistent with ultrastructural observations
232 that show (*i*) numerous waste receptacles within neuronal somata and their association with electron-dense
233 cellular waste (Fig 3H), and (*ii*) the dense obstruction of neuronal somata with waste receptacles in AD-
234 affected human brain tissue that is often associated with cytoplasmic depletion (Fig 3H, J). In contrast,
235 neurons in non-AD affected human hippocampus show small numbers of waste receptacles and intact
236 cytoplasmic structure (Fig 3I).

237 Functional evidence for AQP4-mediated waste intake into 238 ependymal tanycytes

239 To further test our hypothesis that the observed electron-dense material observed in tanycyte-derived waste
240 receptacles is internalized cellular matter, we have investigated fluorochrome uptake by ependymal glial
241 cells in living mouse hippocampus. Within 30 min of exposure to culture medium to which Cy3-conjugated
242 goat anti-rabbit antibody was added, the above-described tanycytes and associated ring structures with
243 emanating receptacles appear brightly fluorescent (Fig 4). In contrast, control preparations that were void
244 of the fluorochrome lacked fluorescence. These findings are consistent with our hypothesis that the
245 fluorochrome may be internalized by these ependymal tanycytes (Fig 4). The ventricular lining showed a
246 fluorescing, interconnected network of tanycyte processes and canals each containing two small-diameter

247 fluorescent channels within their lumina (Fig 4D insets). These canals project into the adjacent ventricular
248 lumen (Fig 4E, bottom inset). To confirm that the internalized fluorochromes are indeed the Cy3 goat-anti
249 rabbit antibodies, we have immunolabeled these brains with an Alexa 488-coupled donkey-anti goat
250 antibody. The double-labeled nature of fluorescent structures (Fig 4A-C) aligns with our postulation that the
251 fluorescence observed within ependymal tanycytes is indeed due to the uptake of the Cy3 conjugated
252 antibody. Interestingly, tanycytes that border directly onto the ventricle form apical canals that project into
253 the ventricular space (Fig 4A). To investigate our hypothesis that the observed internalization of the applied
254 fluorochrome is AQP4-mediated, we have conducted additional experiments in which we have separated
255 and sectioned the two hemispheres of mouse brains. The brain sections of one hemisphere served as
256 control and were kept in culture medium only, the experimental sections from the second hemisphere were
257 immersed in culture medium that contained 60 μM of the selective AQP4-blocker TGN-020. Both
258 hemispheres were then exposed to the Cy3-conjugated antibody. Analysis of these preparations revealed
259 a significantly reduced fluorescent signal within TGN-020-exposed brain cells compared to the controls in
260 comparable brain areas (Fig 4E-F). Comparisons of Log_{10} mean cellular object pixel intensities demonstrate
261 significantly higher pixel intensity in control (0 μM; -1.888) compared to AQP4-blocked (60 μM TGN-020; -
262 2.278) conditions (Fig 4G). Fluorescence was absent in nearby neurons. We postulate that the observed
263 fluorescence in tanycytes may originate from tanycyte-derived, strongly fluorescent receptacles that
264 internalized waste from extracellular spaces. As demonstrated in Fig 4I, the fluorescent structures strongly
265 resemble in shape and size the receptacles visualized with Luxol Blue H&E stain, Aβ, and AQP4/myelin
266 immunolabeling in both human and mouse hippocampus.

267 Waste-receptacle associated gene expression in tanysomes

268 Based on our findings, we postulate that AQP4 and Aβ may be two important functional and structural
269 proteins that are expressed by tanysomes in swell bodies where receptacle formation takes place. We
270 postulate that AQP4 may mediate a convective bulk flow toward the receptacles to flush cellular debris
271 toward these proposed waste-internalizing structures. We further postulate that the role of Aβ may be the
272 structural stabilization of these receptacles to prevent their collapse during the uptake process. We
273 hypothesize that glial fibrillary acid protein (GFAP) may play an important role in the formation of waste

274 receptacles. Since transport of large amounts of structural proteins through narrow tanycyte processes
275 would likely lead to their obstruction we investigated whether these proteins may be expressed by
276 tanysomes in swell bodies where receptacle formation is observed. To evaluate this hypothesis, we have
277 employed RNA-scope gene expression testing AQP4-, GFAP-, Pres1-, and APP-RNA expression in swell-
278 bodies and associated tanysomes throughout human hippocampus. We have furthermore conducted
279 immunohistochemical labeling for Aβ, APP, Pres1 and AQP4 to test if the expressed proteins are detected
280 along waste receptacles. As demonstrated in Figs 5 and 6 both approaches show strong gene expression
281 for all tested probes in swell-bodies. Size, appearance, and location of the structures that show both gene
282 expression and immunolabeling are consistent with tanysomes and their associated toroids and receptacles
283 described above (Figs 2, 5, 6). Interestingly, the distribution of GFAP-RNA appeared less restricted to swell-
284 bodies compared to AQP4-, APP- and Pres1-RNA, which may indicate the transport of GFAP-RNA within
285 tanycyte processes. Immunolabeling for APP, Pres1, AQP4 and Aβ is present along waste receptacles
286 consistent with the gene expression patterns. Interestingly, the comparatively low level of Pres1-RNA
287 expression at tanysome-derived receptacles (Fig 6 G, M) compared to the stronger APP-RNA signal (Fig
288 6H, N) is consistent with the signal strengths observed in Pres1/APP immunolabeled preparations (Fig 6V
289 Pres1; 6X APP). Neuronal cell bodies and somata that are consistent with the appearance of astrocytes
290 appeared consistently unstained (Fig 5). Not all tanysomes showed gene expression, which is consistent
291 with our observations in Aβ-immunolabeled preparations (Fig 7E) and may be due to various stages of
292 differentiation and maturation. Closer investigation of Aβ-immunolabeled swell-bodies shows the
293 emergence of membranous receptacles from strongly Aβ-immunoreactive toroids (Fig 6Q, R). These
294 observations are consistent with ultrastructural investigation of swell bodies that show the emergence of
295 receptacles from myelinated cell processes (Figs 6 S, T, U Ai; 7P; 8D, E). The electron-dense appearance
296 of some of these receptacles at the ultrastructural level is consistent with our postulation of waste uptake.
297 Our hypothesis that this waste may be enzymatically catabolized by caspases is supported by the
298 homogenous appearance of this waste and anti-caspase2 and 3 immunolabeling both of which show strong
299 immunolabeling in receptacle-containing swell bodies (Fig 6Z, Ai).

300 **Amyloid β plaques in AD-affected human hippocampus are**
301 **consistent with hypertrophic tanysome-derived waste**
302 **receptacles**

303 To test our hypothesis that Aβ-plaques in AD-affected hippocampus may originate from hypertrophic waste
304 receptacles that emanate from swell-bodies we have investigated anatomical characteristics of Aβ-
305 immunolabeling in human hippocampus.

306 In AD-unaffected brain tissue modest Aβ-immunolabeling along tanysome-derived waste receptacles was
307 observed. Consistent with our Luxol H&E-stained preparations, immunolabeled receptacles were frequently
308 observed within swell-bodies and projecting into neuronal somata (Fig 7A, D). Similarly, only weak anti-tau
309 staining was observed around waste receptacles in swell-bodies (Fig 7B). In contrast, immunolabeling of
310 AD-affected hippocampus showed strong immunolabeling for both proteins. Similar observations were
311 made in AD-affected brain tissue stained for anti-α-tubulin (see discussion). Compared with non-AD
312 affected brain tissue, the labeled receptacles appeared denser and more hypertrophic in AD-affected tissue
313 giving them the typical appearance of Aβ-plaques (Fig 7). Although the strong Aβ labeling of hypertrophy
314 toroids and receptacles observed in AD-affected tissue makes recognition of labeled structures difficult,
315 their association with tanysomes and swell-bodies is clearly visible (Fig 7 I, J). We have provided
316 complementary histological and ultrastructural images together with schematic drawings to explain the
317 structures that stain for tau-, Aβ-, and α-tubulin proteins (Fig 8). As described earlier, tanysomes in swell-
318 bodies give rise to myelinated receptacles (Figs 2, 7). These findings are consistent with our ultrastructural
319 investigations that show waste receptacles emanating from myelinated cell profiles (Figs 6, 7, 8). Fig 8 D,
320 E demonstrates that strands of receptacles emerge from clearly visible pores in myelinated processes. The
321 GFAP-like fibrillary structures that emerge from the myelinated processes differentiate into numerous
322 bulging waste receptacles with increasing distance from the myelinated process (Fig 8 D, E). The distal
323 ends of these receptacle strands merge into distal ring structures that form within this intricate membrane
324 network and can be seen pulling out of neuronal somata and swell-bodies (Fig 8A). Strong anti-tau
325 immunolabeling and fibrillary structures commonly described as 'intracellular tau tangles' are formed by

326 these swelling myelin-derived circular structures that unravel and form numerous strands of waste
327 receptacles (Fig 8H, I, J). Please note, the electron-dense appearance of the depicted waste receptacles
328 strands in Fig 8D, E, compared with those shown in Fig 6T that are in the forming process. These
329 observations are suggestive of waste internalization within fully formed receptacles depicted in Fig 8.
330 Systematic analysis of anti-tau immunolabeled AD-affected hippocampus shows that anti-tau
331 immunoreactivity is strongest within neuronal somata (Fig 8B). However anti-tau immunoreactive
332 tanysome-associated toroids and receptacles can be observed throughout the hippocampal formation (Figs
333 8, 9). Please note the 'unraveling' of numerous receptacle strands from anti-tau-stained toroids (Figs 7L,
334 M, Q; 8H, I) in AD-affected tissue. Higher zoom of waste receptacles in Aβ-immunolabeled human
335 hippocampus reveals an intricate network of fine canal structures that: (*i*) connect the centrally located
336 toroid-shaped ring structure with emanating waste receptacles, and (*ii*) project from waste receptacles into
337 the surrounding space (Fig 8K). We propose that these structures are part of this waste-internalizing
338 system, and that Aβ may play an important role in the structural stabilization of these canals to prevent their
339 collapse during waste intake (see discussion).

340 Tanycyte-associated hypertrophic pathologies of human 341 hippocampus in AD-affected brain tissue

342 Comparisons between AD-unaffected and AD-affected brain tissue demonstrate that structural
343 abnormalities in the latter are consistently associated with swelling tanycyte processes. Structural
344 differences between tanycyte processes in the alveus are particularly apparent in anti-tau labeled and Luxol
345 H&E-stained preparations (Fig 9A-F). In non-AD affected tissue tanycytes and swell-bodies with associated
346 tanysomes often project in parallel fashion. Although tanysomes form receptacles, they are only weakly
347 stained for tau-protein (Fig 9B, C). In contrast, AD-affected tanycytes appear spongiform, due to the
348 formation of numerous circular structures and bulging waste receptacles that emanate from tanysomes (Fig
349 9D-F, M, N). The heavily myelinated and swelling nature of these tanycyte-derived ring structures is evident
350 in Luxol H&E-stained brain sections (Fig 9D, inset, M). The comparatively strong Tau-immunolabelling in
351 AD-affected brain tissue is predominantly associated with tanysomes, swelling toroids and associated

352 receptacles (Fig 9D-E, O, P). Similar hypertrophic abnormalities can be observed in swell-bodies (Fig 9I-
353 L), neurons (Fig 9G, H) and tanycyte processes (Fig 9M, N, O, R). We repeatedly observed tanycyte
354 swelling associated with bulging receptacles in the vicinity of brown deposits along tanycytes, the
355 appearance of which is consistent with cellular waste (Fig 9J).

356 Based on the findings presented here, we propose that ependymal tanycytes give rise to a dense network
357 of cell processes that form swell-bodies (Fig 10). Swell bodies contain tanycyte-derived AQP4-, GFAP-,
358 Pres1-, and APP-expressing tanysomes from which a membranous network of toroids and receptacles
359 emanate. Whereas some receptacles project into cell somata, others project into extracellular spaces.
360 Based on our functional experiments, we postulate that swell-bodies, and waste receptacles form functional
361 units that are part of a vast glial cell network which internalizes and removes intra- and extracellular waste
362 from the brain in an AQP4-dependent manner (Fig 10). We postulate that waste is flushed toward the
363 receptacles through the formation of an AQP4-mediated convective flow toward the receptacles (Fig 11).
364 We propose that Caspases 2 and 3 may play an important role in waste catabolism. We postulate that
365 hypertrophic swelling of this tanycyte-derived waste canal system leads to obstruction and depletion of
366 neuronal somata culminating in gliaptosis (macroglia-induced cell death).

367 Discussion

368 Our findings support previous findings that myelinated ependymal tanycytes form waste-internalizing
369 receptacles [11]. We describe specialized waste-internalizing organelles that consist of: (*i*) swell-bodies, (*ii*)
370 nucleus-like tanysomes, and (*iii*) tanysome-derived toroids and waste receptacles that are structurally
371 stabilized by Aβ. We postulate that these organelles play important roles in waste clearance from the
372 hippocampal formation.

373 Anatomical and functional significance of swell-bodies and
374 waste receptacles

375 Our light- and electron-microscopic findings shown here strongly support the formation of waste
376 internalizing receptacles. We propose that swell-bodies and associated tanysomes form discrete
377 compartments that govern the differentiation of AQP4-, Caspase 2 and 3, and Aβ-expressing waste
378 receptacles. These findings are consistent with previously reported findings where we have shown the
379 Pres1-immunoreactivity along tanycyte processes that project into neuronal somata where they express
380 APP [11]. The expression of these proteins in swell-bodies that are distant from the associated ependymal
381 tanycyte somata are likely important to ensure rapid and consistent availability of waste internalizing
382 structures throughout the stratum pyramidale. Our observation that not all swell bodies show gene
383 expression suggests that swell bodies may be highly dynamic structures that are continuously formed. This
384 proposed mechanism poses the question how gene expression and receptacle formation within swell-
385 bodies may be governed. Interestingly, in developmental processes gene expression is predominantly
386 governed by localized paracrine factors, calcium signaling, and concentration gradients. It is thus feasible
387 that differences in extracellular signaling factors and swelling patterns may promote or inhibit the
388 differentiation of receptacles. In this context, increased swelling that results in changing concentration
389 gradients may favor receptacle differentiation. We stress to investigate previous observations by Jo et al.
390 regarding the synergistic regulation of swelling patterns in retinal glial cells by AQP4 and the transient
391 receptor potential isoform 4 (TRPV4) channel [15, 16]. It is feasible that this swelling-sensitive calcium-
392 permeable cation channel triggers gene expression in swell-bodies that leads to the differentiation of waste
393 receptacles whose slender processes may be stabilized by Aβ to prevent collapse during waste intake. This
394 hypothesis would be consistent with the excessive formation of swelling Aβ-immunoreactive waste
395 receptacles in AD-affected brains shown here.

396 Fluorochrome uptake by tanycytes

397 While we acknowledge the limitations of the fluorochrome internalization in living mouse brain, we have
398 included these experiments to further support our histological and ultrastructural findings. The observed
399 fluorescence in ependymal tanycytes is consistent with our predictions of AQP4-mediated waste
400 internalization by these cells. The fluorescent structures observed in single optical confocal sections are
401 consistent with (i) shape, (ii) size and (iii) location of receptacles observed in immunohistochemical and

402 histological human brain sections. We do not dispute that future experiments are required and should
403 include the work with organotypic brain cultures and fluoro-nanogold that will enable us to conduct
404 correlative light and ultrastructural investigations. We propose to further test the role of other brain-
405 expressed AQP-subunits including AQP1 and 9 [17].

406 Proposed functions of tau protein and Aβ

407 Amyloid β

408 In both AD-affected and -unaffected hippocampus waste receptacles are *Aβ-immunoreactive*. The
409 structural clarity of Aβ-lined waste receptacles is inconsistent with the currently proposed random
410 accumulation of misfolded Aβ-aggregates [18]. We postulate that receptacles are important for waste
411 removal from the brain in an AQP4-mediated manner. One *key requirement* for such a system is the
412 structural stability of the waste-internalizing components to prevent their collapse during waste intake. One
413 comparable example is tracheal cartilaginous rings that prevent tracheal collapse during respiration. We
414 postulate that Aβ provides similar structural stability to waste-internalizing structures. Investigations
415 regarding the structural architecture of Aβ have revealed the formation of very stable cylindrical amyloid
416 fibrils, consistent with Aβ-immunoreactive fibrils at waste receptacles shown here [13].

417 Tau protein

418 Besides the structural stability of waste-internalizing structures, a second requirement for the proposed
419 waste removal system is the appropriate formation of waste-internalizing receptacles. Too few receptacles
420 may not sufficiently remove cellular waste, whereas too many receptacles may lead to excessive depletion
421 and cell damage as demonstrated in spider CNS [11]. Our observations of anti-tau labeling demonstrate
422 that the formation of characteristic 'tau tangles' is consistently associated with the 'unraveling' of myelinated
423 tanycyte processes that give rise to both intraneuronal and extracellular strands of waste receptacles.
424 Interestingly, previous observations in degenerating spider brain demonstrated that individual myelin
425 sheaths are anchored to microtubules in the form of 'microtubule-associated-breaking points' [11]. The
426 proposed functional significance of these structures is the regulated release and gradual availability of
427 myelin-derived waste-internalizing glial canals. We propose to investigate whether microtubules may have

428 a similar regulatory function regarding the release of waste receptacles. It is feasible that the receptacle
429 release may be governed by tau protein through regulation of the dynamic instability of microtubules. Such
430 processes would be uniquely suitable for the 'on-demand' release of waste receptacles throughout the
431 brain. This would also explain our observations of weak anti-tau labeling in the vicinity of waste receptacles
432 in non-AD-affected brain tissue. Here, we would expect the physiologically appropriate release of waste
433 receptacles. It is feasible that stabilizing functions of microtubules fail in AD due to high intracellular
434 pressure in swelling tanycytes resulting in unraveling of myelinated tanycyte profiles that leads to excessive
435 obstruction and depletion of neuronal somata shown here. The strong co-localization of tanycyte-derived
436 waste receptacles with α-tubulin shown here supports this hypothesis. We propose that such processes
437 take place both in intra- and extracellular places. As demonstrated here, extracellular tanycyte-derived
438 myelin ring structures that unravel are generally less conspicuous compared to their intraneuronal
439 counterparts. It is likely for this reason that tau-tangles have been predominantly associated with
440 intraneuronal locations [19].

441 Proposed role of GFAP

442 The role of GFAP in the formation of waste-internalizing canal structures and their interactions with
443 microtubules is unclear. Three observations lead us to suggest that GFAP may play an important role in
444 waste receptacle formation. (*i*) The strong GFAP gene expression in tanysomes and derived waste
445 receptacles. (*ii*) The strong resemblance of the canal structures that emanate from pores in myelin-rings
446 with the described ultrastructural appearance of GFAP [20]. (*iii*) The abundance of GFAP-RNA in tanycyte
447 processes throughout the hippocampal formation. We propose that GFAP may be a key structural protein
448 for the formation of waste-internalizing receptacles.

449 Tanycyte hypertrophy

450 We propose that tanycyte-related swelling may be caused by ingestion of toxins that likely accumulate in
451 tanycytes and may damage these waste-internalizing glial cells. Consistent with this hypothesis are
452 reported case studies showing onset of chemotherapy-induced leukoencephalopathy, a brain condition
453 associated with spongiform abnormalities and loss of myelin [21].

454 Due to the severe hypertrophy in tanycytes that contain waste obstructions we postulate that swelling may
455 be due to the blockage of drainage canals by insufficiently catabolized waste. This may explain the high
456 incidence of AD-patients impacted by infections [22-25]. The chitin-based structural architecture of fungal
457 pathogens may not be sufficiently catabolized by endogenous enzymes prior to uptake into narrow tanycyte
458 processes. Evidence in support of this hypothesis is demonstrated in a study by Alfonso et al. that illustrates
459 the presence of fungal proteins in tanycyte-like processes, see Figs 3 and 4 in [26]. This would also explain
460 the higher prevalence of AD among women compared to men [27] as women are more prone to fungal
461 infections.

462 Identification of astrocytes, oligodendrocytes, and axonal 463 processes

464 Our RNA-scope experiments show that tanycyte-derived swell bodies that contain tanysomes and waste
465 receptacles show gene expression for GFAP and AQP4. The appearance of these organelles is markedly
466 different from characteristically mononucleated astrocytes that show structured cytoplasmic content.
467 Interestingly, immunohistochemical investigations of human cortical structures identified as astrocytes
468 depict structures that strongly resemble tanysomes and associated waste receptacles shown here, see Fig
469 1 [28]. We have observed similar inconsistencies regarding myelination and oligodendrocytes. As
470 demonstrated here at the electron-microscopic level, myelin-derived strands of waste receptacles protrude
471 from clearly myelinated cell profiles. Until recently, myelination has been associated exclusively with
472 oligodendrocytes and axonal processes for the purpose of axonal insulation. It has also not escaped our
473 attention that the structures we describe as swell-bodies are often referred to as oligodendrocyte somata
474 or satellite cells whose electron-lucent 'fried-egg' appearance is attributed to fixation artifacts [29, 30]. We
475 clearly demonstrate, at both light and electron microscopic levels, that swell bodies do not have a cytoplasm
476 or organelles that are observed in adjacent neuronal and glial somata. We show however, that swell-bodies
477 are AQP4 positive and contain waste-internalizing, electron dense receptacles that emanate from tanycyte-
478 associated tanysomes. Our findings that these receptacles express both AQP4-RNA and GFAP-RNA
479 further supports our hypothesis that these structures may indeed represent tanycyte-derived organelles.

480 Further evidence is provided by our observations that tanycytes in the ependymal lining show identical
481 expression patterns. In contrast, oligodendrocytes are reportedly AQP4-negative [31].

482 Fixation artifact versus functional structure

483 Imperfections in myelin are often attributed to fixation artifacts [32, 33]. However, several arguments
484 indicate that myelin-protrusions are likely of functional significance. (*i*) Our observations of fluorochrome-
485 internalizing receptacles in living mouse brain show that swelling protrusions exist in living fluorochrome
486 internalizing brain tissue. (*ii*) Myelinated tanycyte processes are consistently more spongiform in
487 degenerating brain tissue, including perfused spider and rodent brain [11, 34]. (*iii*) Aquaporin-mediated
488 swelling of cells is not novel. This phenomenon was demonstrated in frog oocytes that received AQP1-
489 water channel cRNA. The resulting water influx into the eggs induced swelling and bursting of the cells [35].
490 Characteristic swell patterns of AQP-expressing cells are utilized to develop AQP-agonists and antagonists
491 [36]. (*iv*) We demonstrate the structural integrity of waste receptacle strands that emanate from well-
492 preserved pores in myelinated human tanycytes consistent with our light-microscopic findings. (*v*)
493 Spongiform pathologies of brain tissue in neurodegeneration have been widely accepted as a hallmark in
494 neurodegenerative diseases including both Creutzfeldt-Jakob Disease and AD [25, 37, 38].

495 Prevention of ion leakage from receptacle-containing neurons

496 Neuronal signal transduction depends on the integrity of electrochemical ion gradients. Holes in the
497 neuronal membrane are therefore detrimental to signal transduction. Interestingly, swell-bodies in non-AD
498 affected brain tissue form visibly concave indentations in the neuronal somata likely due to hydrostatic
499 pressure associated with fluid-filled swell-bodies. The resulting tight association between the neuronal and
500 swell-body membranes may thus effectively seal the point of tanycyte entry into neurons and prevent
501 leakage flow.

502 Conclusions

503 We acknowledge that the glial-canal-hypothesis presented here contradicts current understanding of
504 structure in neuroscience. We have thus provided numerous picture panels to support our statements. We

505 have countless additional supportive experiments, images and data that are too extensive to include into
506 one manuscript. We are happy to provide access to our preparations, technology, data and images to the
507 neuroscience community and strongly encourage the independent re-investigation of cellular structure in
508 the human and mammalian nervous system by other investigators. We suggest that particular focus should
509 be given to the identity of myelinated cell profiles using ultrastructural serial section analysis to
510 unambiguously demonstrate the origin of myelinated cell processes in the brain.

511 # Acknowledgements

512 The authors would like to thank Melanie Winters and Shane Grandusky for assistance with the uptake
513 experiments. We thank Dr. John DeWitt for support and access to human decedent tissue. We thank Drs.
514 Alain Brizard, Christopher Francklyn, Mark Nelson, Mark Lubkowitz, Douglas Taatjes, and Heather Driscoll
515 for support and helpful feedback on this work. We thank Ann and Dr. David MacLaughlin for their donation
516 to fund the Zeiss confocal microscope. The Electron Microscopic investigations were performed at the
517 Microscopy Imaging Center at the University of Vermont (RRID: SCR_018821). We thank Natalie Cashen,
518 Dr. Gerald Herrera, Nicole Bouffard, Kyra Lee, and Brad Vietje for technical support.

519

References

1. Agre P, King LS, Yasui M, Guggino WB, Ottersen OP, Fujiyoshi Y, et al. Aquaporin water channels – from atomic structure to clinical medicine. Journal of Physiology. 2002;542(1):3-16. doi: 10.1113/jphysiol.2002.020818.
2. Iliff JJ, Wang M, Liao Y, Plogg BA, Peng W, Gundersen GA, et al. A paravascular pathway facilitates CSF flow through the brain parenchyma and the clearance of interstitial solutes, including amyloid β. Science Translational Medicine. 2012;4(147):147ra11. Epub 2012/08/17. doi: 10.1126/scitranslmed.3003748. PubMed PMID: 22896675; PubMed Central PMCID: PMCPMC3551275.
3. Barichello de Quevedo JL, Leffa DT, Pascoal TA. Glymphatic system waste clearance and Alzheimer's disease. Braz J Psychiatry. 2023;45(5):385-6. Epub 20230525. doi: 10.47626/1516-4446-2023-0049. PubMed PMID: 37229609; PubMed Central PMCID: PMCPMC10894633.
4. Buccellato FR, D'Anca M, Serpente M, Arighi A, Galimberti D. The Role of Glymphatic System in Alzheimer's and Parkinson's Disease Pathogenesis. Biomedicines. 2022;10(9). Epub 20220913. doi: 10.3390/biomedicines10092261. PubMed PMID: 36140362; PubMed Central PMCID: PMCPMC9496080.
5. Murdock MH, Yang CY, Sun N, Pao PC, Blanco-Duque C, Kahn MC, et al. Multisensory gamma stimulation promotes glymphatic clearance of amyloid. Nature. 2024;627(8002):149-56. Epub 20240228. doi: 10.1038/s41586-024-07132-6. PubMed PMID: 38418876; PubMed Central PMCID: PMCPMC10917684.
6. Iliff JJ, Nedergaard M. Is there a cerebral lymphatic system? Stroke. 2013;44(6 Suppl 1):S93-S5. doi: 10.1161/STROKEAHA.112.678698. PubMed PMID: 23709744.
7. Nedergaard M. Neuroscience. Garbage truck of the brain. Science. 2013;340(6140):1529-30. doi: 10.1126/science.1240514. PubMed PMID: 23812703.
8. Nedergaard M, Goldman SA. Brain Drain. Scientific American. 2016;314(3):44-9. PubMed PMID: edsjsr.26046876.
9. Mestre H, Hablitz LM, Xavier ALR, Feng W, Zou W, Pu T, et al. Aquaporin-4-dependent glymphatic solute transport in the rodent brain. eLife. 2018;7:e40070. Epub 2018/12/19. doi: 10.7554/eLife.40070. PubMed PMID: 30561329; PubMed Central PMCID: PMCPMC6307855.
10. Abbott NJ, Pizzo ME, Preston JE, Janigro D, Thorne RG. The role of brain barriers in fluid movement in the CNS: is there a 'glymphatic' system? Acta neuropathologica. 2018;135(3):387-407. doi: 10.1007/s00401-018-1812-4. PubMed PMID: 29428972.
11. Fabian-Fine R, Weaver AL, Roman AG, Winters MJ, DeWitt JC. Myelinated Glial Cells: Their Proposed Role in Waste Clearance and Neurodegeneration in Arachnid and Human Brain. J Comp Neurol. 2024;532(11):e70000. doi: 10.1002/cne.70000. PubMed PMID: 39610046; PubMed Central PMCID: PMCPMC11605019.
12. Maarouf CL, Daugs ID, Spina S, Vidal R, Kokjohn TA, Patton RL, et al. Histopathological and molecular heterogeneity among individuals with dementia associated with Presenilin mutations. Mol Neurodegener. 2008;3:20. Epub 20081120. doi: 10.1186/1750-1326-3-20. PubMed PMID: 19021905; PubMed Central PMCID: PMCPMC2600784.
13. Tycko R. Amyloid polymorphism: structural basis and neurobiological relevance. Neuron. 2015;86(3):632-45. doi: 10.1016/j.neuron.2015.03.017. PubMed PMID: 25950632; PubMed Central PMCID: PMCPMC4425266.
14. Stirling DR, Swain-Bowden MJ, Lucas AM, Carpenter AE, Cimini BA, Goodman A. CellProfiler 4: improvements in speed, utility and usability. BMC Bioinformatics. 2021;22(1):433. Epub 20210910. doi: 10.1186/s12859-021-04344-9. PubMed PMID: 34507520; PubMed Central PMCID: PMCPMC8431850.
15. Jo AO, Ryskamp DA, Phuong TT, Verkman AS, Yarishkin O, MacAulay N, et al. TRPV4 and AQP4 Channels Synergistically Regulate Cell Volume and Calcium Homeostasis in Retinal Muller Glia. J Neurosci. 2015;35(39):13525-37. doi: 10.1523/JNEUROSCI.1987-15.2015. PubMed PMID: 26424896; PubMed Central PMCID: PMCPMC4588615.
16. Liedtke W, Friedman JM. Abnormal osmotic regulation in trpv4-/- mice. Proc Natl Acad Sci U S A. 2003;100(23):13698-703. Epub 20031027. doi: 10.1073/pnas.1735416100. PubMed PMID: 14581612; PubMed Central PMCID: PMCPMC263876.

17. Badaut J, Fukuda AM, Jullienne A, Petry KG. Aquaporin and brain diseases. Biochim Biophys Acta. 2014;1840(5):1554-65. Epub 20131026. doi: 10.1016/j.bbagen.2013.10.032. PubMed PMID: 24513456; PubMed Central PMCID: PMCPMC3960327.
18. Gupta A, Goyal R. Amyloid beta plaque: a culprit for neurodegeneration. Acta Neurol Belg. 2016;116(4):445-50. Epub 20160427. doi: 10.1007/s13760-016-0639-9. PubMed PMID: 27118573.
19. Trejo-Lopez JA, Yachnis AT, Prokop S. Neuropathology of Alzheimer's Disease. Neurotherapeutics. 2022;19(1):173-85. Epub 20211102. doi: 10.1007/s13311-021-01146-y. PubMed PMID: 34729690; PubMed Central PMCID: PMCPMC9130398.
20. Nahirney PC, Tremblay M-E. Brain ultrastructure: putting the pieces together. Frontiers in cell and developmental biology. 2021;9:629503.
21. Moore-Maxwell CA, Datto MB, Hulette CM. Chemotherapy-induced toxic leukoencephalopathy causes a wide range of symptoms: a series of four autopsies. Mod Pathol. 2004;17(2):241-7. doi: 10.1038/modpathol.3800049. PubMed PMID: 14704718.
22. Bruno F, Abondio P, Bruno R, Ceraudo L, Paparazzo E, Citrigno L, et al. Alzheimer's disease as a viral disease: Revisiting the infectious hypothesis. Ageing Research Reviews. 2023;91. doi: 10.1016/j.arr.2023.102068. PubMed PMID: S1568163723002271.
23. Mancuso R, Sicurella M, Agostini S, Marconi P, Clerici M. Herpes simplex virus type 1 and Alzheimer's disease: link and potential impact on treatment. Expert review of anti-infective therapy. 2019;17(9):715-31. doi: 10.1080/14787210.2019.1656064. PubMed PMID: 31414935.
24. Sait A, Angeli C, Doig AJ, Day PJR. Viral Involvement in Alzheimer's Disease. ACS chemical neuroscience. 2021;12(7):1049-60. doi: 10.1021/acschemneuro.0c00719. PubMed PMID: 33687205.
25. Sigurdson CJ, Bartz JC, Glatzel M. Cellular and Molecular Mechanisms of Prion Disease. Annual review of pathology. 2019;14:497-516. doi: 10.1146/annurev-pathmechdis-012418-013109. PubMed PMID: 30355150.
26. Alonso R, Pisa D, Marina AI, Morato E, Rábano A, Rodal I, et al. Evidence for fungal infection in cerebrospinal fluid and brain tissue from patients with amyotrophic lateral sclerosis. International Journal of Biological Sciences. 2015;11(5):546.
27. Niu H, Alvarez-Alvarez I, Guillen-Grima F, Aguinaga-Ontoso I. Prevalence and incidence of Alzheimer's disease in Europe: A meta-analysis. Neurologia. 2017;32(8):523-32. Epub 20160426. doi: 10.1016/j.nrl.2016.02.016. PubMed PMID: 27130306.
28. Forrest SL, Kim JH, Crockford DR, Huynh K, Cheong R, Knott S, et al. Distribution Patterns of Astrocyte Populations in the Human Cortex. Neurochem Res. 2023;48(4):1222-32. Epub 20220805. doi: 10.1007/s11064-022-03700-2. PubMed PMID: 35930103; PubMed Central PMCID: PMCPMC10030423.
29. Komori T. Pathology of oligodendroglia: An overview. Neuropathology. 2017;37(5):465-74. Epub 20170526. doi: 10.1111/neup.12389. PubMed PMID: 28548216.
30. Garman RH. Histology of the central nervous system. Toxicol Pathol. 2011;39(1):22-35. Epub 20101130. doi: 10.1177/0192623310389621. PubMed PMID: 21119051.
31. Amiry-Moghaddam M, Ottersen OP. The molecular basis of water transport in the brain. Nature Reviews Neuroscience. 2003;4(12):991-1001.
32. Möbius W, Cooper B, Kaufmann WA, Imig C, Ruhwedel T, Snaidero N, et al. Electron microscopy of the mouse central nervous system. Methods in cell biology. 96: Elsevier; 2010. p. 475-512.
33. Möbius W, Nave K-A, Werner HB. Electron microscopy of myelin: Structure preservation by high-pressure freezing. Brain Research. 2016;1641(Part A):92-100. doi: 10.1016/j.brainres.2016.02.027. PubMed PMID: 2016-11609-001.
34. Fabian-Fine R, Aiken AM, Aug JR, Boucher JD, Butler DC, Clancy LJ, et al. Neurodegeneration in a novel invertebrate model system: Failed microtubule-mediated cell adhesion and unraveling of macroglia. Journal of Comparative Neurology. 2023;531(5):618-38. Epub 2023/01/04. doi: https://doi.org/10.1002/cne.25450. PubMed PMID: 36594894.
35. Preston GM, Carroll TP, Guggino WB, Agre P. Appearance of Water Channels in Xenopus Oocytes Expressing Red Cell CHIP28 Protein. Science. 1992;256(5055):385-7. PubMed PMID: edsjsr.2877088.
36. Wang S, Solenov EI, Yang B. Aquaporin inhibitors. Aquaporins: Springer; 2023. p. 317-30.
37. Smith TW, Anwer U, DeGirolami U, Drachman DA. Vacuolar change in Alzheimer's disease. Arch Neurol. 1987;44(12):1225-8. doi: 10.1001/archneur.1987.00520240007003. PubMed PMID: 3314815.

625 38. Whatley BR, Li L, Chin LS. The ubiquitin-proteasome system in spongiform degenerative
626 disorders. Biochim Biophys Acta. 2008;1782(12):700-12. Epub 20080823. doi:
627 10.1016/j.bbadis.2008.08.006. PubMed PMID: 18790052; PubMed Central PMCID: PMCPMC2612938.

628

629 # FIGURE LEGENDS

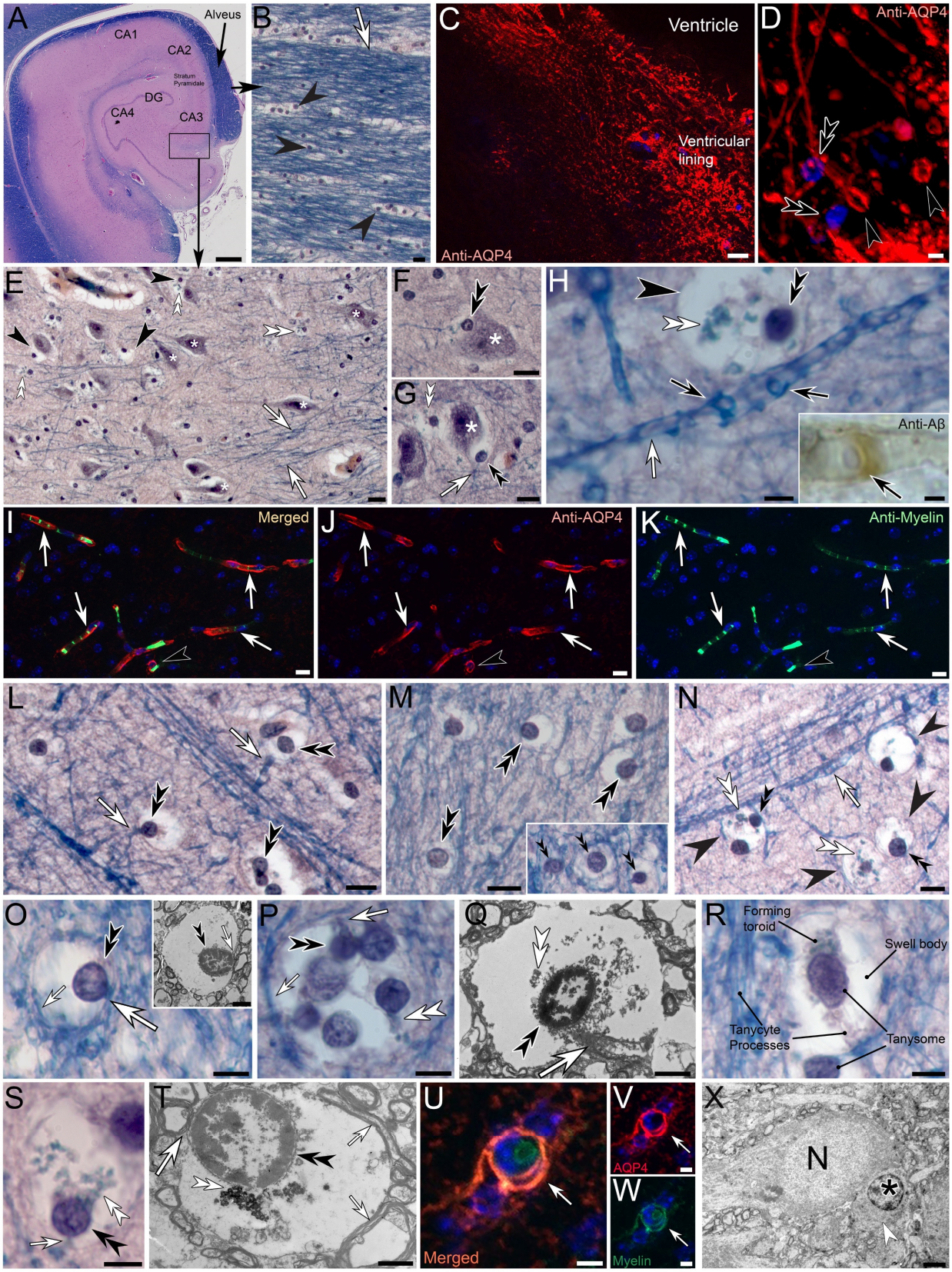
A
Alveus
CA1
CA2
Stratum Pyramidale
DG
CA4
CA3
B
C
Ventricle
Ventricular lining
Anti-AQP4
D
Anti-AQP4
E
F
G
H
Anti-Aβ
I
Merged
J
Anti-AQP4
K
Anti-Myelin
L
M
N
O
P
Q
R
Forming toroid
Swell body
Tanycyte Processes
Tanysome
S
T
U
Merged
V
AQP4
W
Myelin
X
N

630

Fig 1. Myelinated Ependymal tanycytes in human and mouse hippocampus project into the hippocampal stratum pyramidale and give rise to waste-internalizing receptacles. (A-B) The alveus of human hippocampus contains numerous Luxol H&E-stained ependymal tanycytes that send vast numbers of slender myelinated processes (*white arrow in B*) into the stratum pyramidale of the hippocampal formation. Numerous electron-lucent 'swell-bodies' with associated nucleus-like tanysomes are forming along individual myelinated processes (*black arrowheads in B*). **(C, D)** Aquaporin4-immunolabeling of human alveus shows strong immunoreactivity of tanycyte processes. Higher magnification *(D)* shows Hoechst-blue stained nucleus-like structures in close association with tanycytes (*black double arrowheads in D*). Circular, immunoreactive swellings can be observed along the tanycyte processes (*black arrowheads*). **(E-G)** Luxol-blue stained human tanycyte processes (white arrows) project into the stratum pyramidale where they form translucent swell-bodies (black arrowheads) with associated nucleus like tanysomes (*black double arrowheads*). Please note the close association of swell-bodies with neuronal somata (*asterisks*). **(H)** Tanycyte (*white arrow*) with associated translucent swell body (*black arrowhead*) with tanysome (*black double arrowhead*) with emanating waste receptacles (*white double arrowhead*). Swelling ring structures (*black arrows*) that line the inside of swelling tanycyte processes are visible in Luxol H&E-stained and Aβ-immunolabeled (*black arrow in inset*) tanycyte processes. **(I-K)** AQP4 (*red*) and myelin (*green*) immunolabeling of mouse hippocampus shows double labeled tanycyte processes that contain myelin-immunoreactive circular profiles that line the inner lumina of the cell processes (*white arrows*). *Black arrowhead:* AQP4-immunolabled swell body. **(L-N)** Tanycyte processes (*white arrows*) with associated swell-bodies (*black arrowheads*) in human stratum pyramidale. *White double arrowheads:* forming receptacles; *Black double arrowheads:* Tanysomes. *Inset in M*: Forming tanysomes in the alveus. **(O-T)** Structural characteristics of swell bodies, associated tanysomes (*black double arrowheads*) and receptacles (*white double arrowheads*) in human hippocampus. Both light and ultrastructural images show the electron lucent nature of the swell bodies. Each swell body contains between one and 6 tanysomes that are stained for nuclear stain in Luxol H&E-stained preparations and appear associated with myelinated tanycyte processes (*white arrows*). Tanysomes give rise to toroids and receptacles some of which appear electron-dense at the ultrastructural level (*white double arrowheads in T*). Please note the myelinated tanycyte profiles that line the circumference of swell bodies (*small white arrows in O, P, T*). **(U-W)**

659 AQP4/Myelin immunolabeled swell body in mouse hippocampus shows the double-labeled nature of
660 myelinated AQP4-immunoreactive tanycyte profiles (*white arrow*) around the periphery of swell bodies. **(X)**
661 Typical structured appearance of a glial nucleus (*asterisk)* and surrounding cytoplasm (*white arrowhead*).
662 **Scale bars:** A: 500 µm, B:10 µm, C: 20 µm; D: 5 µm; E-G: 10 µm, H: 5 µm, Inset 3 µm; I-N: 10 µm; M: 20
663 µm; N: 10 µm; O: 5 µm, (*Inset*) 2 µm; P: 5 µm Q 2 µm R: 5 µm; S: 5 µm; T: 2 µm; U-W: 5 µm; X: 2 µm.

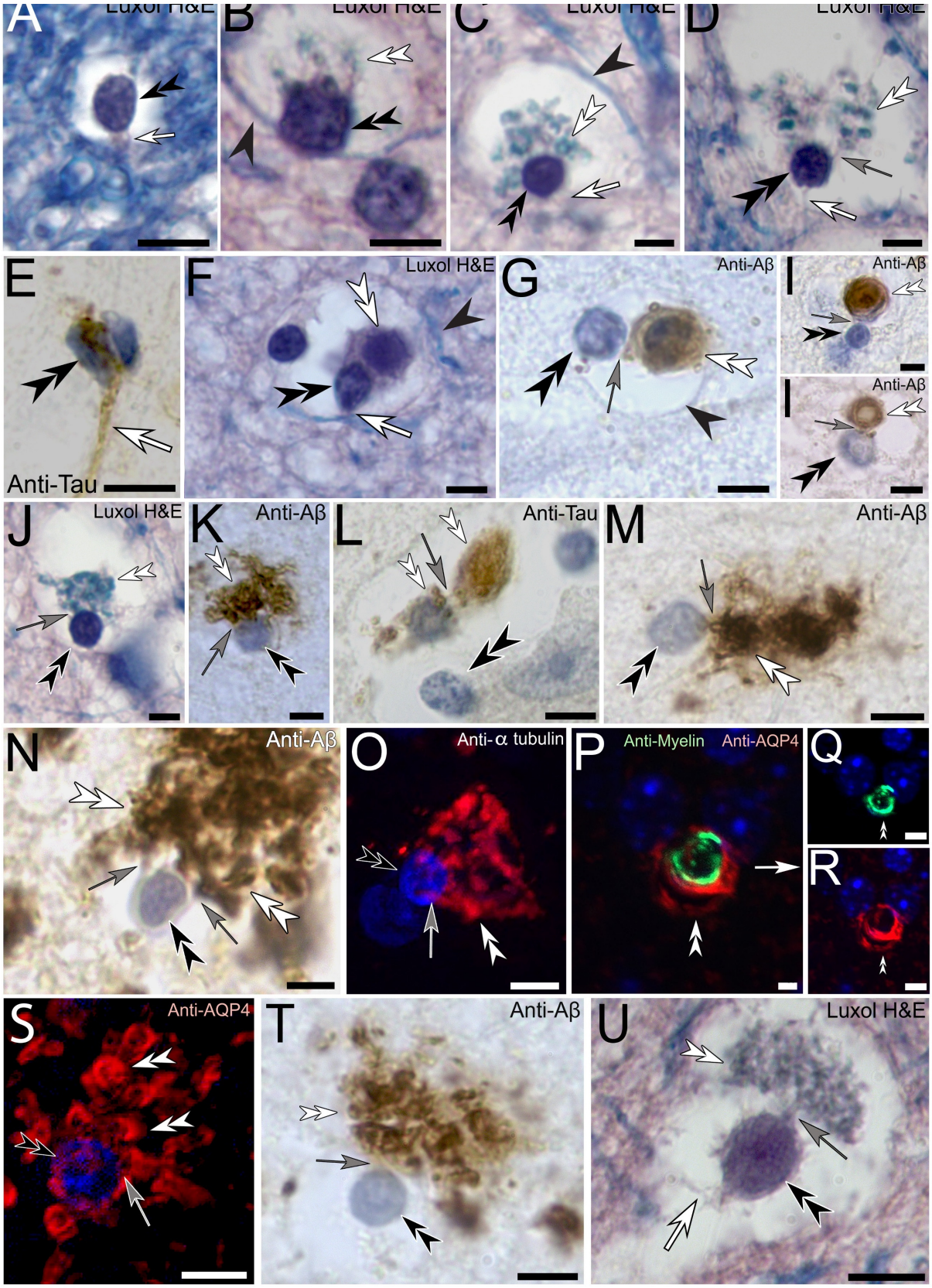
A
Luxol H&E
B
Luxol H&E
C
Luxol H&E
D
Luxol H&E
E
Anti-Tau
F
Luxol H&E
G
Anti-Aβ
I
Anti-Aβ
I
Anti-Aβ
J
Luxol H&E
K
Anti-Aβ
L
Anti-Tau
M
Anti-Aβ
N
Anti-Aβ
O
Anti-α tubulin
P
Anti-Myelin
Anti-AQP4
Q
R
S
Anti-AQP4
T
Anti-Aβ
U
Luxol H&E

664

665 **Fig 2. Tanysomes in human and mouse hippocampus give rise to toroids and receptacles that are**
666 **immunoreactive for Aβ, hyperphosphorylated tau protein, myelin, AQP4 and α-tubulin. (A-O)** Human
667 hippocampal tanysomes within swell-bodies give rise to a network of membranous receptacles and toroids
668 (*white double arrowheads*). The physical attachment between tanysomes (*black double arrowheads*) and
669 tanycyte processes (*white arrows*) and receptacles (*grey arrows*) is clearly visible. Nuclear stain is observed
670 in both tanysomes and emanating toroid-shaped ring structures (*F, G, H*). The tanysome-derived
671 membrane network in human brain is immunoreactive for tau-protein (*E, L*), Aβ (G, *H, I, K, M, N*) and α-
672 tubulin (*O)*. **(P-R)** Immunolabeling of mouse hippocampus for anti-AQP4 (*red*) and myelin (*green*)
673 demonstrates that toroids that emerge from tanysomes are immunoreactive for both epitopes. **(S-U)**
674 Tanysome-derived receptacles in preparations immunolabeled for anti-AQP4 (S), anti-Aβ (T) and stained
675 for Luxol H&E (U) consistently demonstrate their physical association with tanysomes (*grey arrows*). Scale
676 bars: A-U: 5 μm.

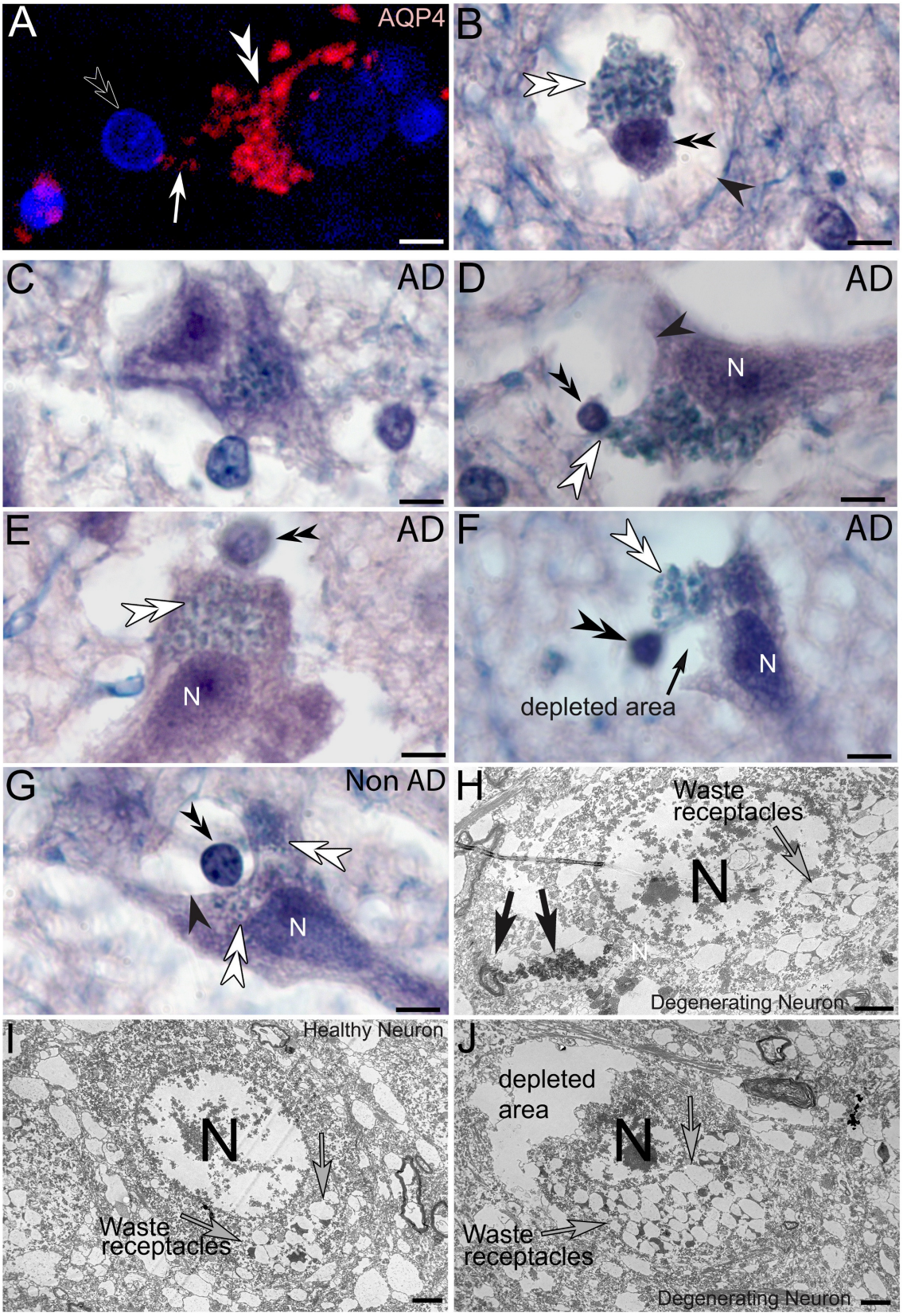
A
AQP4
B
C
AD
D
AD
N
E
AD
N
F
AD
N
depleted area
G
Non AD
N
H
Waste
receptacles
N
N
Degenerating Neuron
I
Healthy Neuron
N
Waste
receptacles
J
depleted
area
N
Waste
receptacles
Degenerating Neuron

677

678 **Fig 3. Tanysome-derived waste receptacles in human hippocampus project into neuronal somata.**
679 **(A)** Tanysome-derived (*black double arrow*) waste receptacles are immuno-positive for aquaporin-4 (*white*
680 *double arrowhead*). **(B-G)** Luxol H&E-stained preparations show the characteristically blue stained
681 tanysome-derived waste receptacles that differentiate in swell-bodies (*panel B*) project into pyramidal cell
682 somata. *Black double arrowhead*s: Tanysomes; *White double arrowhead*s: Waste receptacles; *Black*
683 *arrowheads*: Outer margins of swell-bodies; *N*: Neuronal somata. **(H-J)** Ultrastructural depiction of healthy
684 and degenerating neuronal somata demonstrates the abundance of swelling waste receptacles and gradual
685 depletion of cytoplasmic areas in degenerating somata (*H, J*) compared to the much sparser number of
686 waste receptacles in a healthy neuron that shows an intact cytoplasmic structure (*I*). Please note the waste
687 accumulation associated with a waste receptacle strand that emanates from a myelinated cell profile
688 (arrows in H) consistent with strands of waste receptacles observed at the light microscopic level (C-G).
689 Scale bars: A-G: 5 μm; H-J: 2 μm.

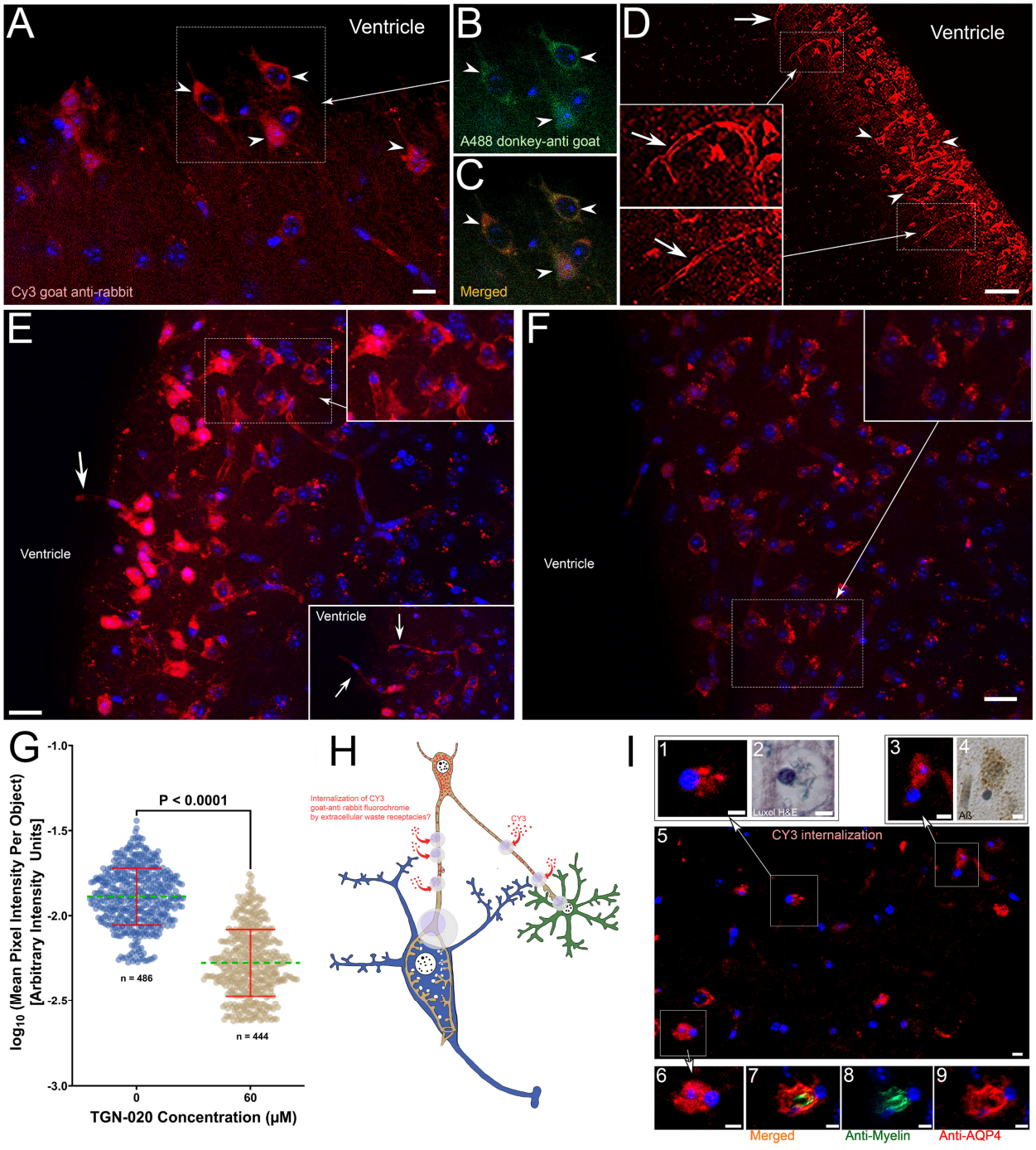

690

691 **Fig 4. Evidence for aquaporin-4-dependent Cy3 goat anti-rabbit antibody internalization into living**
692 **mouse hippocampal ependymal tanycytes. (A-C)** Living ependymal tanycytes that were exposed to Cy3
693 goat anti rabbit antibody appear fluorescent after 30 min exposure (*white arrowheads in A*). Immunolabeling
694 against goat-protein using an Alexa 488-coupled donkey-anti-goat antibody demonstrates co-localization
695 of both Cy3 and Alexa 488 fluorochromes (*white arrowheads in B, C*) indicative that the red fluorescence

696 within tanycytes originates from internalized Cy3 goat anti rabbit antibody. **(D)** Ependymal tanycytes in
697 mouse alveus show red fluorescence after 30 min exposure of living brain tissue to Cy3 goat anti-rabbit
698 antibody (*white arrowheads*). A fine network of fluorescing processes (*grey arrowhead*) is visible in the
699 stratum pyramidale. *Insets:* Canal structures each containing two fluorescing channels (arrows) are
700 frequently observed projecting into the adjacent ventricle. **(E, F)** Normalized intensity of internalized Cy3
701 fluorochrome comparing control (0; *E*) and AQP4-blocked (60 μM TGN-020; *F*) conditions. Control cells
702 demonstrate a higher pixel intensity, especially towards the alveus. **(G)** Log_{10} mean cellular object intensity
703 is significantly larger in control (0 μM; -1.888) compared to AQP4-blocked (60 μM TGN-020; -2.278; $t(928)$
704 $= 32.666$, $p = 2.44 \times 10^{-156}$, unpaired two-tailed *t*-test). Inset in E: Fluorescent canal structures extending
705 into the ventricle (white arrows). **(H)** Schematic depiction of the proposed waste internalization
706 demonstrated here. We postulate that living tanycytes internalize surrounding fluorochromes via
707 extracellular waste receptacles that are formed within swell-bodies explaining the observed fluorescence
708 in ependymal tanycytes. To visualize cells, Hoechst blue nuclear stain was applied after fixation of the
709 brains. **(I)** Single 3- μm optical confocal section of mouse brain with internalized fluorochromes. Note the
710 strong resemblance of brightly fluorescent tanysome-like areas (*1, 3, 5, 6*) with toroid- and receptacle-
711 forming human tanysomes (*2, 4*) and AQP4/myelin-doublelabeled mouse tanysomes (*7-9*). Scale bars: A-
712 C: 10 μm, D: 50 μm; E, F: 20 μm; H: not drawn to scale; I: 5 μm.

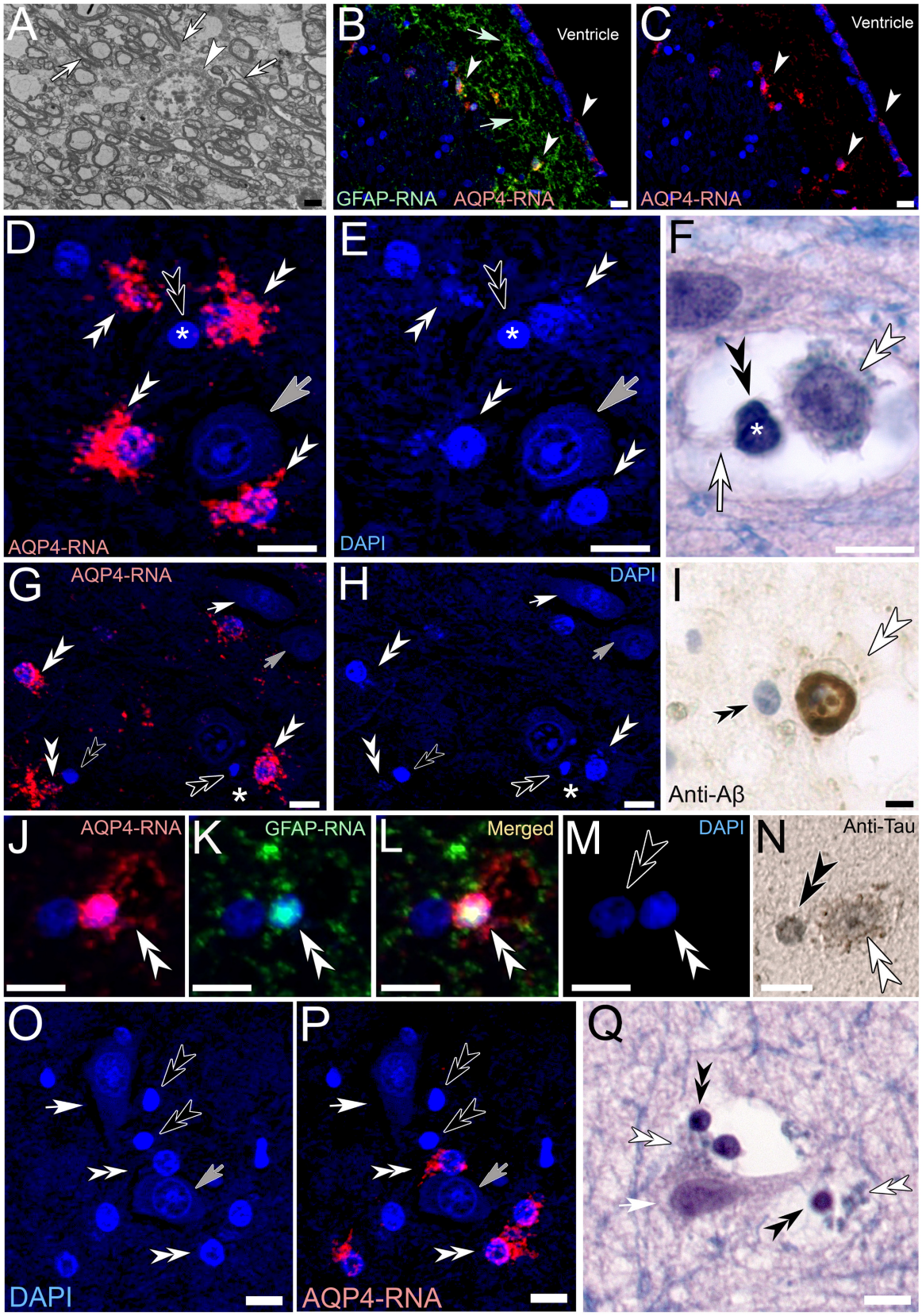
A
B
Ventricle
GFAP-RNA
AQP4-RNA
C
Ventricle
AQP4-RNA
D
AQP4-RNA
E
DAPI
F
G
AQP4-RNA
H
DAPI
I
Anti-Aβ
J
AQP4-RNA
K
GFAP-RNA
L
Merged
M
DAPI
N
Anti-Tau
O
DAPI
P
AQP4-RNA
Q

713

714 **Fig 5: RNA-scope gene expression within tanycytes and associated swell-bodies of human**
715 **hippocampus in both AD-affected and AD-unaffected tissue. (A)** Electron micrograph of a tanycyte
716 soma (*white arrowhead*) in the alveus of AD-affected tissue shows myelinated tanycyte processes
717 projecting from the soma (*white arrows*). **(B, C)** RNA-scope visualization of RNA expression for glial-
718 fibrillary acid protein (GFAP; *green*) and aquaporin-4 (AQP4; *red*) demonstrate the expression of both RNAs
719 in the alveus (white arrowheads). Please note the abundance of GFAP within tanycyte processes indicative
720 of RNA-transport (green arrows). **(D, E)** AQP4-RNA expression in the stratum pyramidale counter-stained
721 with DAPI nuclear stain shows brightly fluorescing tanysomes (*black double arrowheads*) with emerging
722 waste receptacles (*white double arrowheads*). Please note the absence of staining in the astrocyte-like cell
723 soma (*grey arrows*). **(F)** Luxol H&E stained tanysome (black arrowhead) with emerging receptacle-forming
724 toroid (white double arrowhead) strongly resembles the AQP4-expressing tanysome indicated by the
725 *asterisk in D, E*. **(G, H)** AQP4-expressing waste receptacles (*white double arrowheads*) that emerge from
726 tanysomes (*black double arrowheads*). Cell somata resembling a neuron (*white arrow*) and adjacent
727 astrocyte (*grey arrow*) are void of AQP4-RNA expression. **(I)** Tanysome (*black double arrowhead*) with
728 emerging anti Aβ-stained toroid (*white double arrowheads*) strongly resembles the AQP4-RNA expressing
729 tanysome indicated by the *asterisks in G, H*. **(J-M)** Receptacle-forming (*white double arrowheads*)
730 tanysome (*black double arrowheads*) show co-expression for GFAP (*green, white double arrowheads*) and
731 AQP4 (*red*). **(N)** Anti-tau-stained tanysome (*black double arrowhead*) with associated receptacle-forming
732 toroid (*white double arrowheads*) strongly resemble the tanysome shown in *J-M*. **(O-P)** AQP4-RNA
733 expression is restricted to receptacle-forming tanysomes (*white and black double arrowheads*) that are in
734 close contact to an unstained neuronal soma (*white arrow*) and an unstained astrocyte-like soma (*grey*
735 *arrow*). **(Q)** Luxol H&E-stained pyramidal cell soma (*white arrow*) shows the consistency of the RNA-scope
736 labeling in *O, P* whereby receptacle forming tanysomes (*white and black double arrowheads*) are adjacent
737 to neuronal soma. **Scale Bars:** A: 2 μm; B, C: 5 μm; D-H: 10 μm; I: 5 μm; J-Q: 10 μm.

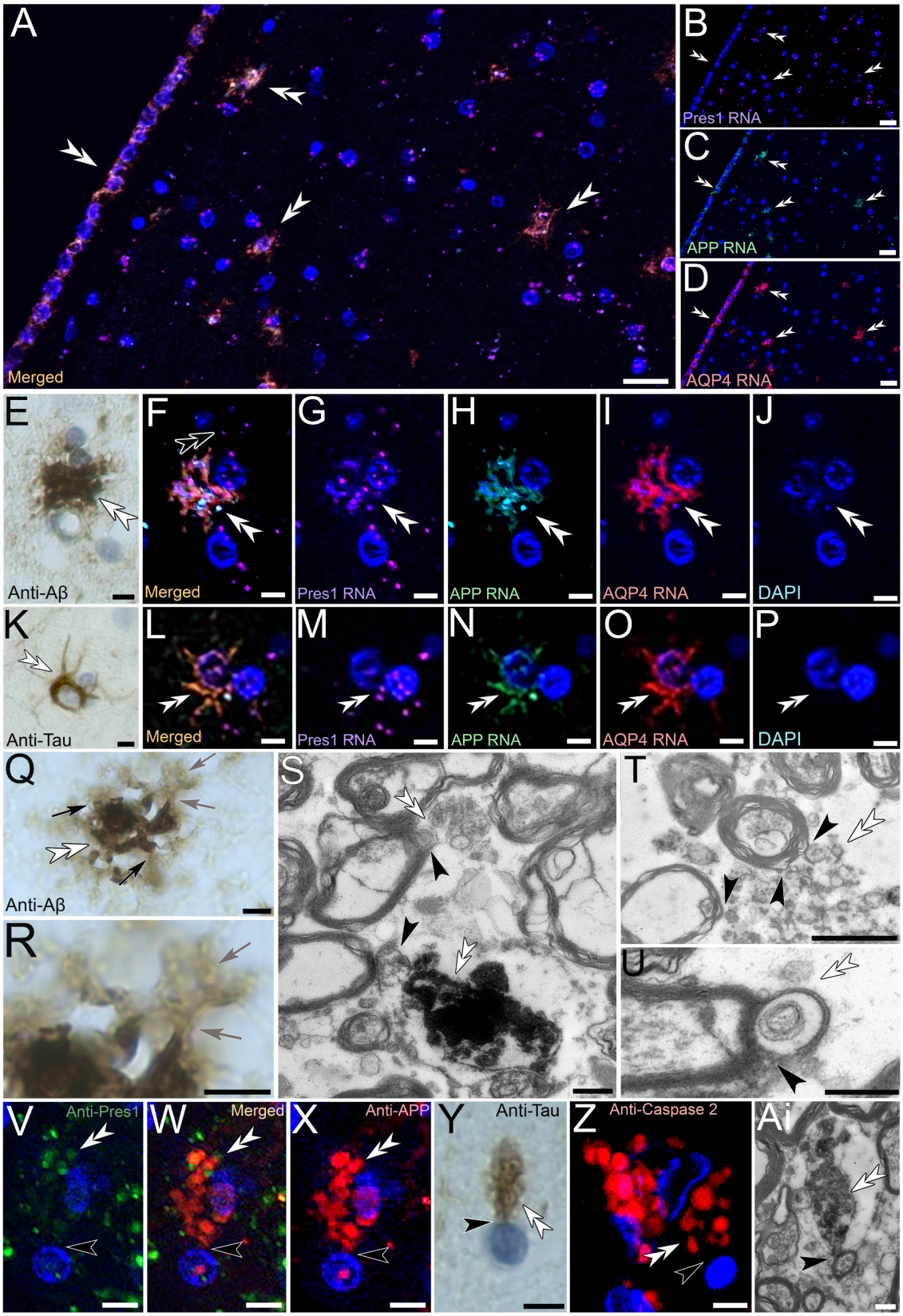
A
Merged
B
Pres1 RNA
C
APP RNA
D
AQP4 RNA
E
Anti-Aβ
F
Merged
G
Pres1 RNA
H
APP RNA
I
AQP4 RNA
J
DAPI
K
Anti-Tau
L
Merged
M
Pres1 RNA
N
APP RNA
O
AQP4 RNA
P
DAPI
Q
Anti-Aβ
R
S
T
U
V
Anti-Pres1
W
Merged
X
Anti-APP
Y
Anti-Tau
Z
Anti-Caspase 2
Ai

738

739 **Fig 6. Amyloid β-related gene expression in AD-affected human hippocampus. (A-D, F-J, L-P)**
740 Ependymal tanycytes in the ventricular lining show RNA-co-expression for Presenilin-1 (*Pres-1*, *magenta*),
741 Amyloid Precursor Protein (*APP*, *green*) and Aquaporin 4 (*AQP4*, *red*). Higher magnification (*F-J, L-P*)
742 shows that gene expression is associated with tanysome-derived toroids and receptacles (*DAPI nuclear*
743 *stain*). **(E)** Tanysome-associated waste receptacles are strongly Aβ-immunoreactive (*white double*
744 *arrowheads*) consistent with observed Pres1 and APP gene expression shown in *F-J*. **(K)** Anti-tau
745 immunoreactive tanysome-associated toroid. **(Q, R)** Anti Aβ-immunoreactive toroid (white double
746 arrowhead) with emerging waste receptacles (*black and grey arrows*). Grey arrows indicate the area shown
747 at higher zoom in (*R)*. **(S-U)** Electron micrographs of forming waste receptacles (*white double arrowheads*)
748 in swell-bodies that emerge from myelinated cell profiles (*black arrowheads*). (V-Ai) Tanysome-associated
749 waste receptacles show immunolabeling for Pres1 (V, W), APP (W, X), Tau protein (Y) and Caspase 2 (Z).
750 The appearance of the immunolabeled receptacles is consistent with the ultrastructural appearance of
751 waste-containing receptacles (Ai). **Scale Bars:** A-D: 20 μm; E-R: 5 μm; S: T: U: 2 μm; V-Z: 5 μm; Ai: 500
752 nm.

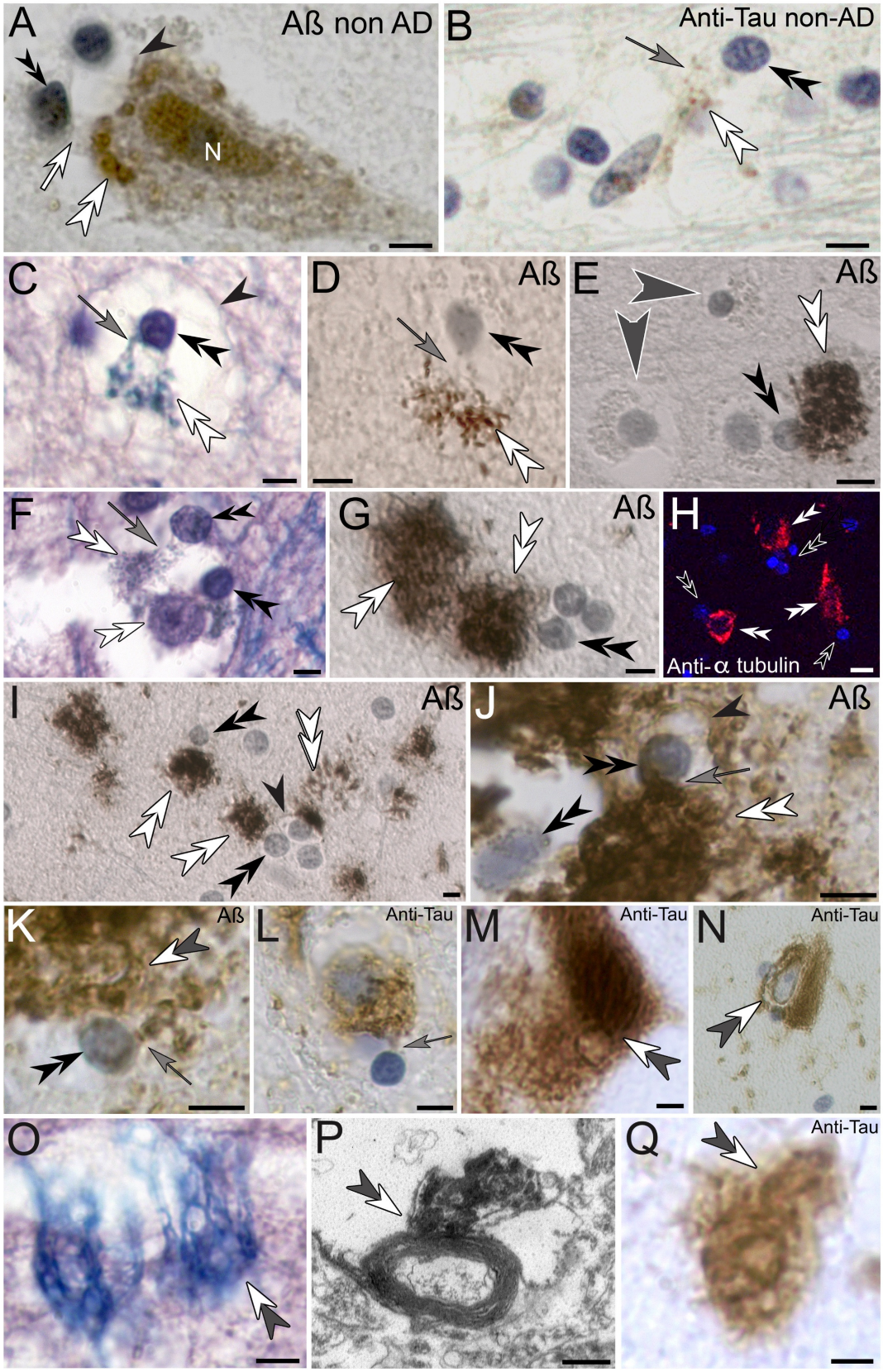
A
Aß non AD
N
B
Anti-Tau non-AD
C
D
Aß
E
Aß
F
G
Aß
H
Anti-α tubulin
I
Aß
J
Aß
K
Aß
L
Anti-Tau
M
Anti-Tau
N
Anti-Tau
O
P
Q
Anti-Tau

753

754 **Fig 7. Tanysome-derived waste receptacles stain for Aβ, tau protein, and α-tubulin in AD-affected**
755 **human brain tissue (A-B)** Alzheimer Disease unaffected brain tissue shows moderate immunolabeling for
756 Aβ and tau protein in association with intraneuronal (*A*) and extracellular (*B*) waste receptacles. Generally,
757 the signal for Aβ is stronger compared to the observed anti-tau immunolabeling. **(C-Q)** Comparison of Luxol
758 H&E-stained tanysome-derived receptacles and unraveling Luxol blue-stained ring structures in AD-
759 affected brain tissue (*C, F, O*) demonstrates their structural similarities to Aβ immunolabeled (*D, E, G, I, J,*
760 *K*), Anti-tau immunoreactive (*L, M, N, Q*) and anti α-tubulin immunolabeled (*H*) preparations. Please note
761 the similarities of unraveling myelin-derived cell profiles of varying sizes (*O*) with unraveling myelinated cell
762 profiles at the ultrastructural level (*P*). These unraveling toroids are consistent with unraveling toroids
763 observed in the anti-tau labeled preparations (*L, M, N, Q*) that have the characteristic appearance of 'tau
764 tangles' (*grey-white double arrowheads*). *Black double arrowhead*s: Tanysomes; *White double arrowhead*s:
765 Forming receptacles; *Black arrowheads*: outer margins of swell-bodies; *N*: Neuronal soma. Scale bars: A-
766 O: 5 μm; P: 500 nm; Q: 3 μm.

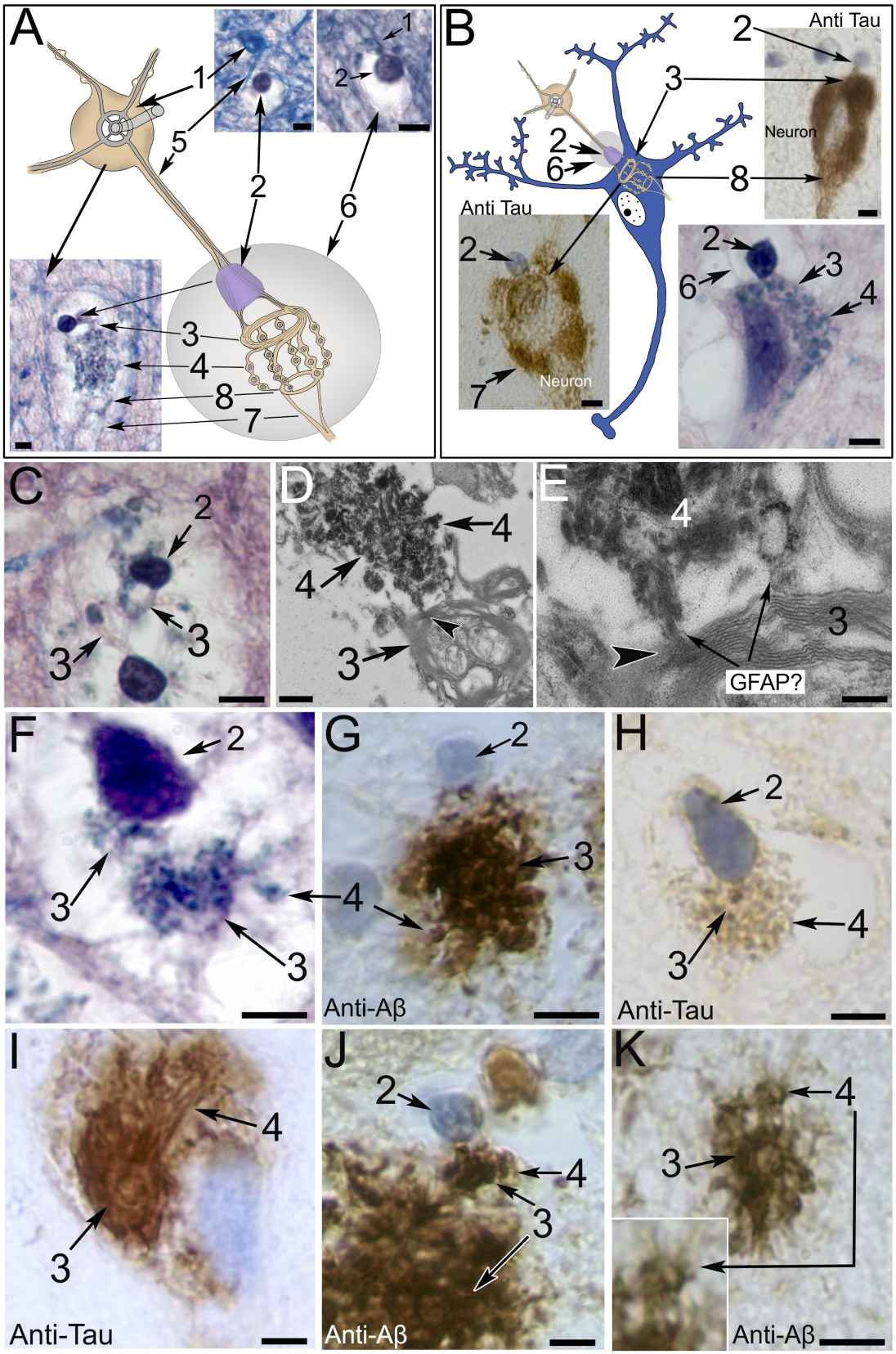
A
1
2
3
4
5
6
7
8
B
Anti Tau
Neuron
C
D
E
GFAP?
F
G
Anti-Aβ
H
Anti-Tau
I
Anti-Tau
J
Anti-Aβ
K
Anti-Aβ

767

768 **Fig 8. Light- and electron-microscopic architecture of tanycyte-derived waste receptacles formed**
769 **within swell bodies in the human brain. (A, B)** Schematic depiction of the proposed structures that form
770 within swell-bodies (*A*) and can be observed to project into neuronal somata (*B*). Swelling toroids (*1*) that
771 are connected to an adjacent tanysome (*2*) via a slender tanycyte process (*5*). The tanysome gives rise to
772 myelinated toroids (*3*) from which strands of waste-internalizing receptacles emerge (*4*). The individual
773 receptacle strands terminate into a distal toroid-shaped ring structure (*8*) that merge into distal tanycyte
774 processes (*7*). **(C-K)** The above-described structures and their proposed Luxol H&E-stained (C, F), anti-
775 tau immunolabeled (*B, H, I*) and anti-Aβ immunolabeled (*G, J, K*) equivalents in AD-affected hippocampus
776 are depicted and labelled accordingly within each panel. The tanysome-derived toroids and associated
777 receptacle strands (*3, 4*) appear electron dense at the ultrastructural level and form large numbers of
778 receptacles (*D, E*). The emerging tubular canal structures resemble glial fibrillary acid protein (*GFAP*, *black*
779 *arrowhead in E*). Waste receptacles can be seen emanating from toroid-shaped ring structures in Luxol
780 H&E-stained preparations (*white arrowhead in F*). Immunolabeling for Aβ shows similar immunolabeled
781 waste receptacles (*G, J, K and inset*). Higher zoom shows the association of individual receptacles with a
782 fine network of fibrillary canals consistent with the postulated stabilization of these proposed waste-
783 internalizing structures by Aβ (*inset in K*). *6*: outer perimeter of swell body; Scale bars in light microscopic
784 images: 5 µm; D: 500 nm; E: 150 nm. Schematic drawings not drawn to scale.

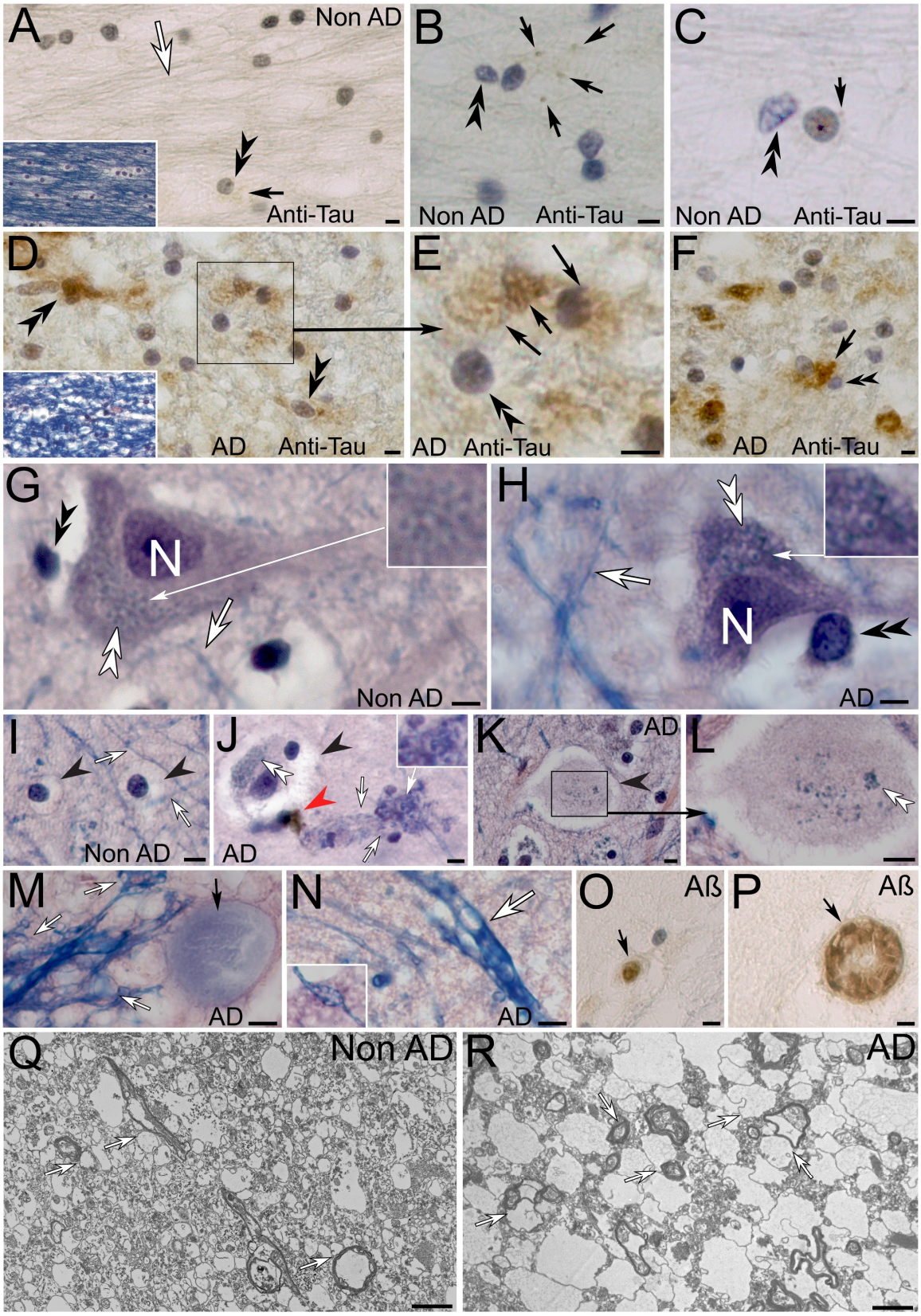
A
Non AD
Anti-Tau
B
Non AD
Anti-Tau
C
Non AD
Anti-Tau
D
AD
Anti-Tau
E
AD
Anti-Tau
F
AD
Anti-Tau
G
N
Non AD
H
N
AD
I
Non AD
J
AD
K
AD
L
M
AD
N
AD
O
Aß
P
Aß
Q
Non AD
R
AD

785

786 **Fig 9. Hypertrophic tanycyte swelling in human AD-affected brain tissue. (A-C)** Tanycyte processes
787 in the alveus (*white arrows*) in non-AD affected brain appear linear and project parallel to each other in both
788 anti-tau labeled brain tissue (*A-C*) and Luxol H&E-stained preparations (*inset in A*). Tanysome (*black double*
789 *arrowheads*) derived waste receptacles are sparse and appear either unlabeled or weakly labeled for tau
790 protein (*black arrows*). **(D-F)** The alveus in AD-affected brain tissue appears spongiform with bulging
791 tanycyte processes in both anti-tau (*D-F*) and Luxol H&E-stained preparations (*inset in D*). Numerous
792 swelling anti-tau labeled waste receptacles (black arrows) emanate from associated tanysomes (*back*
793 *double arrowheads*). **(G, H)** Similar hypertrophic swelling can be observed in tanycyte processes (*white*
794 *arrows in G compared to H*) and intraneuronal tanycyte receptacles (*white double arrowheads in G*
795 *compared to H, higher zoom of receptacles in respective insets*). **(I-N)** Swell bodies and associated tanycyte
796 profiles in non-AD affected tissue appear comparatively small and intact (*I*) compared to those in AD-
797 affected brain tissue (*J-N*). In the latter swell bodies, tanysome-derived waste receptacles and associated
798 tanycytes show abnormal hypertrophy (*J-L*). Please note the accumulation of brown deposit within the
799 hypertrophic tanycyte process, indicative of a blockage by cellular waste (*red arrowhead in J*). Tanysomes
800 and associated waste receptacles are difficult to recognize in swell-bodies that show advanced swelling
801 stages (*K, L higher zoom that visualizes remaining waste receptacles*). Hypertrophic tanycyte processes
802 form numerous swelling circular structures in comparison to those in non-AD affected tissue (*arrows in I*
803 *compared to M, N, inset in N*). **(O, P)** Differences in swelling patterns are also observed in Aβ
804 immunolabeled tanycyte-derived toroids (*arrows in O and P*). **(Q, R)** Comparison between non-AD (*Q*) and
805 AD-affected tissue (*R*) at the ultrastructural level demonstrates abnormal spongiform swelling that
806 originates from bulging myelin-derived tanycyte protrusions, (*white arrows in Q compared to R*). Scale bars:
807 A-P: 5 μm, Q, R: 2 μm.

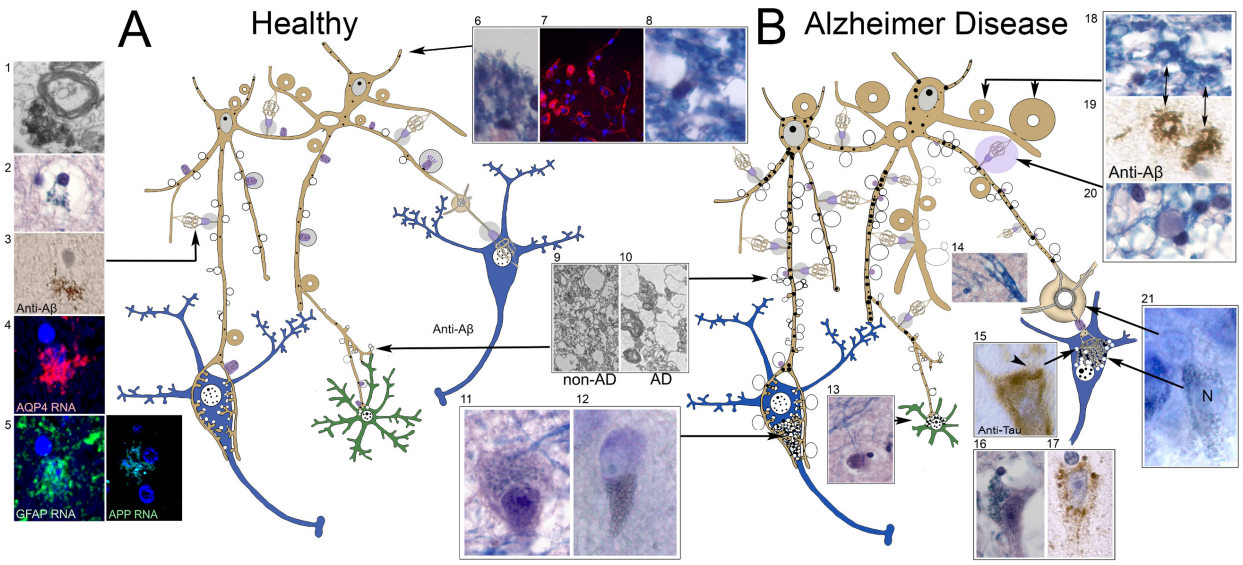

808

809 **Fig 10. Schematic depiction of proposed tanycyte-derived waste canal system in the human**
810 **hippocampus of healthy (A) and AD-affected brain tissue. (A)** Neurons (*blue*) and glial cells (*green*) are
811 contacted by myelinated aquaporin-4-expressing ependymal tanycytes (*beige*). The latter form both
812 swelling toroids and waste receptacles (*1-5*) either directly from tanycyte protrusions [11] or swell-body-
813 derived that internalize and remove cellular waste from the brain parenchyma likely via apical drainage
814 canals (*6-8*) in a proposed AQP4-dependent manner. We propose that receptacle formation is likely
815 dependent on: (*i*) Amyloid β-mediated stabilization to prevent the collapse of waste-internalizing receptacles
816 during this process, and (*ii*) tau-protein for the gradual and time appropriate release of waste receptacles.
817 **(B)** In AD-affected brain tissue, hypertrophic tanycyte abnormalities that may be caused by physical waste
818 obstruction lead to swelling of the tanycytes affecting the brain parenchyma (*9, 10*), intracellular waste
819 receptacles that lead to dense obstruction of affected neurons and glial cells (*11, 12, 13*), tanycyte
820 processes (*14*), and intraneuronal tanysome-derived receptacles (*15, 16, 17*). Swelling of tanycytes in the
821 alveus leads to excessive sprouting of tanycyte-derived waste receptacles that appear Aβ immunoreactive
822 (*18, 19*). Similar swelling can be observed in tanycyte-associated swell-bodies (*20*) and toroids (*21*).
823 Schematics are not drawn to scale.

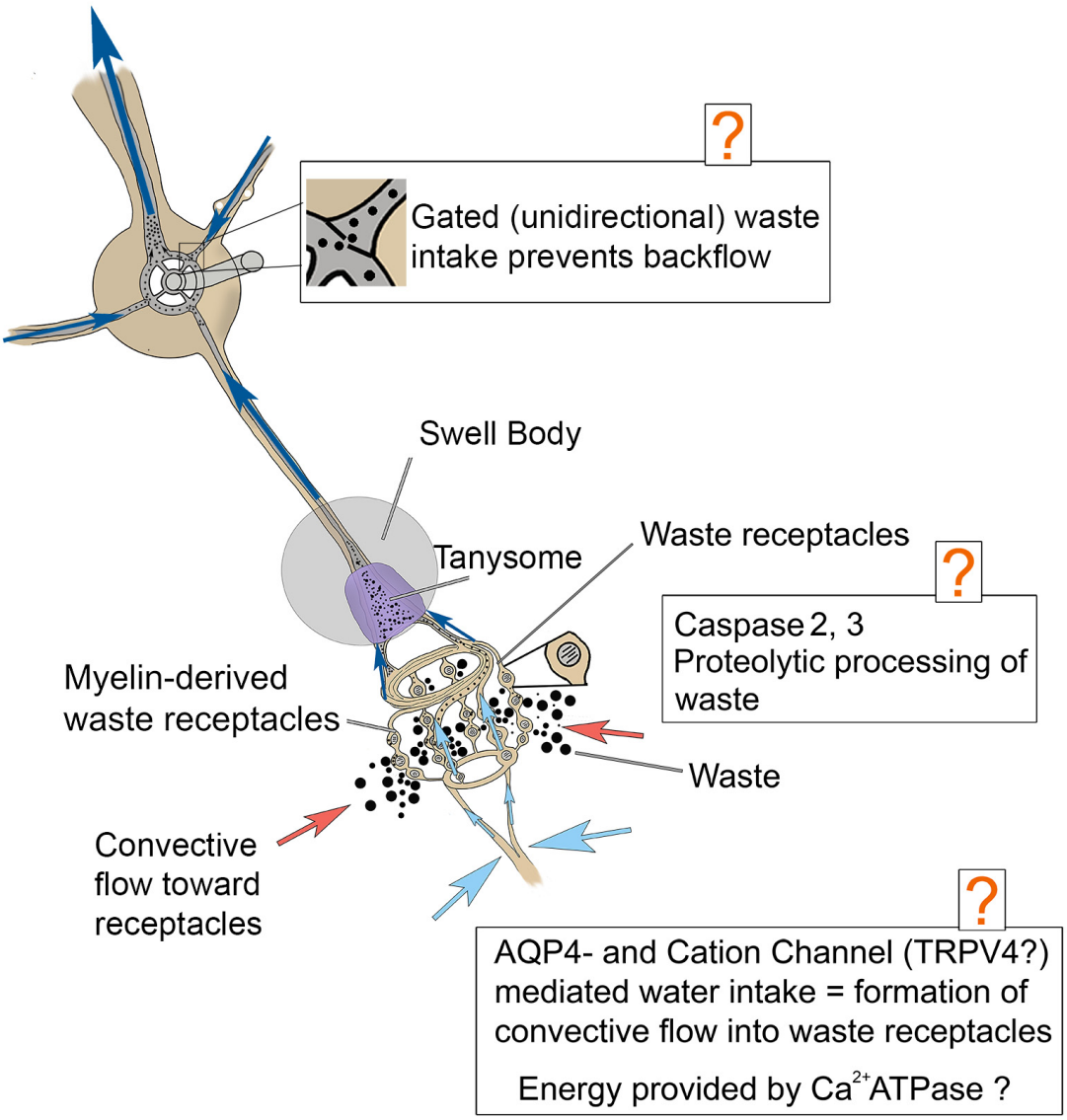

824

825 **Fig 11. Proposed AQP4-mediated uptake mechanism of cellular waste into tanysome-derived waste**
826 **receptacles.** Swell-bodies differentiate myelin-derived AQP4-expressing receptacles that create a
827 convective cytoplasmic flow toward the receptacles (light blue arrows) that flushes cellular debris particles
828 toward the receptacles (red arrows). We postulate that receptacle-associated enzymes (e.g., Caspase 2)
829 catabolize the debris prior to uptake into tanycytes. We propose that water influx into tanycytes may be
830 calcium-mediated through the synergistic activation of TRPV4 cation channels. We postulate that swelling
831 toroids that are formed along tanycytes may draw waste from the receptacles toward the toroids (dark blue
832 arrows). We postulate that these canals may contain membrane-gated valves that prevent backflow.
833 Schematic not drawn to scale.